Structural and effective brain networks in focal epilepsy

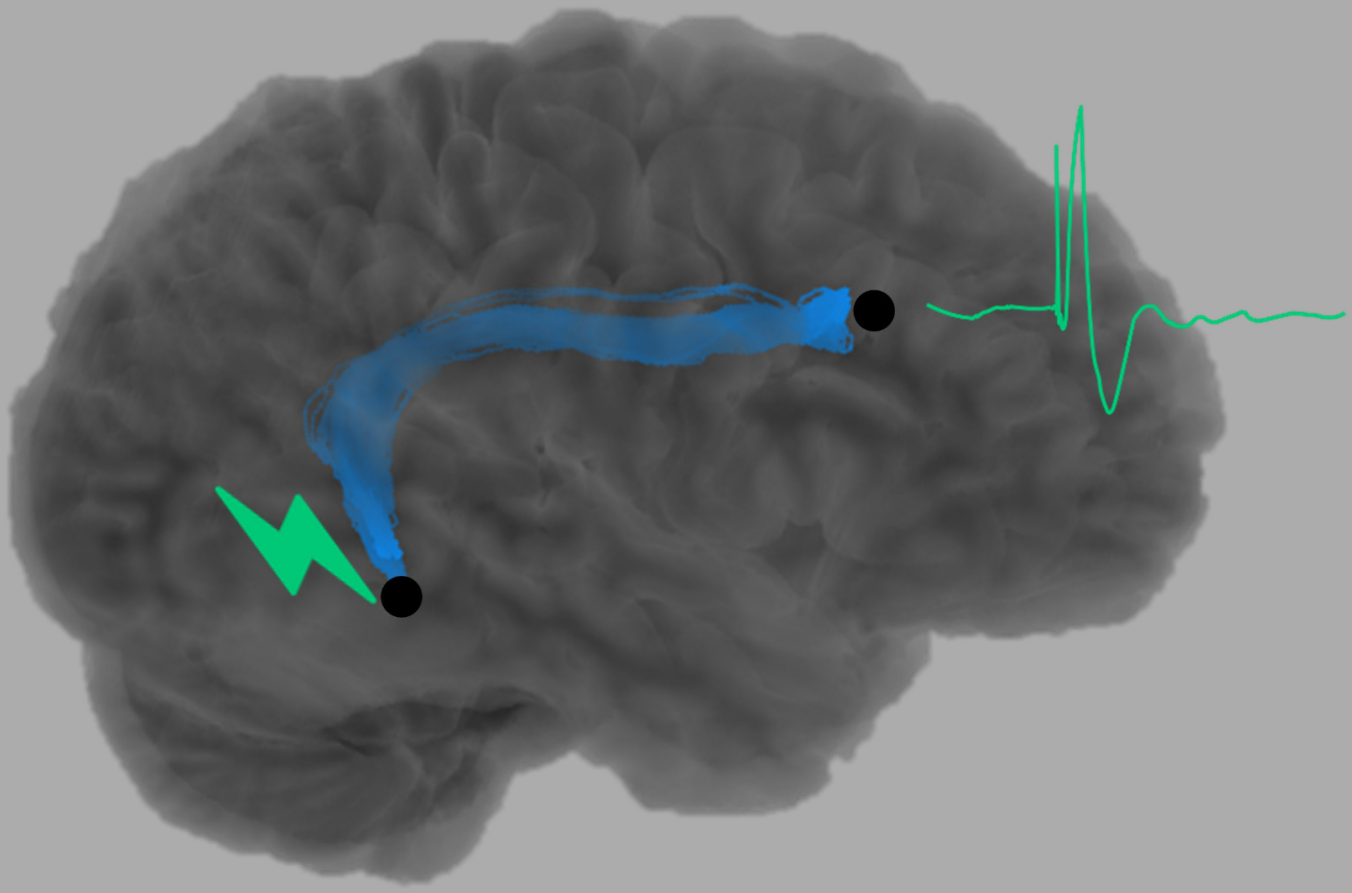

Master Thesis Technical Medicine
Susanne Jelsma

31 October 2022

Structural and effective brain networks in focal epilepsy

Master Thesis Technical Medicine
Department of Clinical Neurophysiology & Epilepsy surgery
University Medical Center Utrecht & University of Twente

Graduation committee

Chairman & Technical supervisor	**Prof.dr.ir. M.J.A.M van Putten** University of Twente Faculty of Science and Technology
Medical & Daily supervisor	**dr. N.E.C. van Klink** University Medical Center (UMC) Utrecht Department of Clinical Neurophysiology and Epilepsy Surgery
Daily supervisor	**D. van Blooijs MSc** UMC Utrecht, Stichting Epilepsie Instellingen Nederland (SEIN)
Medical supervisor	**Prof.dr. M. Zijlmans** UMC Utrecht, Stichting Epilepsie Instellingen Nederland (SEIN)
Process supervisor	**drs. N.S. Cramer Bornemann** University of Twente Faculty of Science and Technology
External member	**L. Rutten MSc** University of Twente Faculty of Science and Technology

Abstract

Introduction: Epilepsy is nowadays regarded as a network disorder instead of a focal disease. While epilepsy surgery is currently based on the removal of a local focus, a network approach seems more suitable and might eventually improve the surgical outcome. Insight into how epilepsy alters the patient-specific brain network is necessary to establish a network based surgical strategy. There are different approaches to characterize brain networks but it is unclear if and to what extent these approaches relate. Effective networks are described by the causal influence between brain areas by invasive perturbation of one of the areas with for example single pulse electrical stimulation (SPES). Structural networks are described by the anatomical connections between brain areas via white matter tracts and can be determined non-invasively with diffusion weighted imaging (DWI). Exploring the relation between structural and effective networks could deepen our understanding of epileptogenic networks by revealing the biologically plausible structural pathways that give rise to effective connections. DWI based structural network characterization is non-invasive and could be adapted earlier in the surgical trajectory than SPES based effective network characterization. The combination of structural and effective networks could potentially elucidate network alterations caused by epilepsy. We aimed to characterize structural networks with DWI and effective networks with SPES, evaluate their relation, and explore how epilepsy alters this relation.

Methods: We compared effective networks acquired by SPES to structural networks derived from DWI. Invasive electroencephalography (iEEG) electrode positions were used as nodes. Early responses (ER) in SPES were automatically detected, for which an existing detection algorithm for ERs in electrocorticography (ECoG) was optimized and validated for stereo EEG (sEEG) (Chapter 2). The optimized detector was used to reconstruct the effective networks. We reconstructed structural networks from DWI and fiber tractography(FT) using the iFOD2 algorithm with parameters optimized for local network structures (Chapter 3). We determined the inter-modal similarity between structural and effective networks with the Jaccard index (JI). We compared the topography with the degree and betweenness centrality on electrode contact level within patients. We constructed a linear multilevel model to evaluate the correlation at group level, accommodate for node proximity bias due to irregular spatial sampling, and analyze the influence of epilepsy.

Results: We included 13 patients (five ECoG, eight sEEG). The sensitivity and specificity of the optimized ER detector were 81% and 93%. The FT algorithm for sEEG and ECoG required equal parameters. The median JI was 0.25 (IQR: 0.19-0.29). The degree of the structural networks compared to the effective networks at patient level showed a significant positive correlation in 10/13 patients. This correlation was also present at group level with linear multilevel modeling after controlling for node proximity. We did not find statistical evidence that epilepsy alters the relation between structural and effective networks.

Conclusion: We explored the relation between structural and effective patient-specific brain networks. The performance of the optimized automatic ER detector was sufficient to reliably characterize effective networks. Structural and effective networks showed a moderate overall relation and their topography, described by the degree correlated independently of common sources of bias. This suggests that for some applications structural and effective networks could be interchangeably used, in which case we recommend to use non-invasive, structural networks. Higher sample sizes and correction of the node proximity on a patient level are needed to exactly explain to what extent structural and effective networks interrelate and further investigate how epilepsy alters this relation. We recommend continuing a multi-modality approach to study complex network alterations in focal drug resistant epilepsy patients to establish a network based surgical strategy.

Contents

List of abbreviations

AP	anterior-posterior
BC	betweenness centrality
CSD	constrained spherical deconvolution
DWI	diffusion weighted imaging
ECoG	electrocorticography
EEG	electroencephalography
EZ	epileptogenic zone
EPI	echo-planar imaging
ER	early responses
ERP	evoked response potential
FNP	false negative percentage
FOD	fiber orientation distribution
FPP	false positive percentage
FT	fiber tractography
ICC	intra class correlation
iEEG	invasive EEG
JI	jaccard index
MRI	magnetic resonance imaging
MSMT-CSD	multi-shell multi-tissue constrained spherical deconvolution
NPV	negative predictive value
PA	posterior-anterior
PPV	positive predictive value
SD	standard deviation
sEEG	stereo EEG
SOZ	seizure onset zone
SPES	single pulse electrical stimulation
STT	streamline tracking technique
SD	standard deviation

1. General introduction

1.1 Clinical Background

Epilepsy is one of the oldest medical topics to write about with notes dating back to 4000 Before the Common Era [1]. Today it is still a popular topic with 10.000 epilepsy-themed articles published in the last year [2]. Not an abnormal number when you look at the characteristics of epilepsy. 1.000 patients of all ages are diagnosed yearly with epilepsy in the Netherlands [3]. An epileptic seizure is caused by hyper synchronized discharges of neurons that disturb normal brain function. This disturbance of brain function can manifest in a variety of clinical signs such as short loss of awareness, unusual behavior, or generalized tonic-clonic seizures. The consequences of seizures are severe and include a shorter life expectancy, neuropsychological impairment, and social disability [4]. The life expectancy of someone with epilepsy is shortened by 2 to 10 years and in 2020, 320 people died with epilepsy as the underlying cause of death [3]. The disease burden is similar to brain cancer and multiple sclerose in the Netherlands. The severity of these consequences relates to seizure control [3]. In thirty percent of the epilepsy patients, seizure freedom is not achieved with drug therapy [5].

Patients with focal, drug resistant epilepsy may benefit from epilepsy surgery, but 25-50% of the surgical candidates do not become seizure-free [6]. Epilepsy surgery is based on the removal of the epileptogenic zone (EZ). The EZ is the brain area that must be removed to achieve seizure freedom [7]. In most patients, the EZ is delineated with the integration of non-invasive techniques including video electroencephalography (EEG), magnetic resonance imaging (MRI), functional MRI, magnetoencephalography, and ^{18}F-fluorodeoxyglucose positron emission tomography [8]. An invasive EEG (iEEG) monitoring period is indicated for epilepsy surgery candidates with no structural abnormalities observed from imaging, no clearly defined EZ from EEG, dual pathology, or a possible overlap of the EZ with functional areas [9]. iEEG electrodes are placed inside the skull and enable a high spatial resolution recording without extracranial artifacts and signal attenuation from the skull [10]. iEEG electrodes are implanted under anesthesia and the patient is monitored on the ward for 7 to 21 days, during which spontaneous seizures and interictal activity are analyzed to approximate the EZ. Stimulations are performed to determine the functional areas and confirm the EZ. There are two principal iEEG configurations: electrocorticography (ECoG) and stereo EEG (sEEG) (see Figure 1.1). ECoG with subdural electrodes allows contiguous sampling of the lateral cortical surfaces of the cerebral hemispheres to precisely delineate eloquent functional areas and the EZ. sEEG with cylindrical depth electrodes offers the ability to sample deep structures such as the insula or medial and basal surfaces. The choice of iEEG configuration depends on the expected location of the EZ, expected cooperation of deep structures, and the desire to contiguous sample the cortical surface.

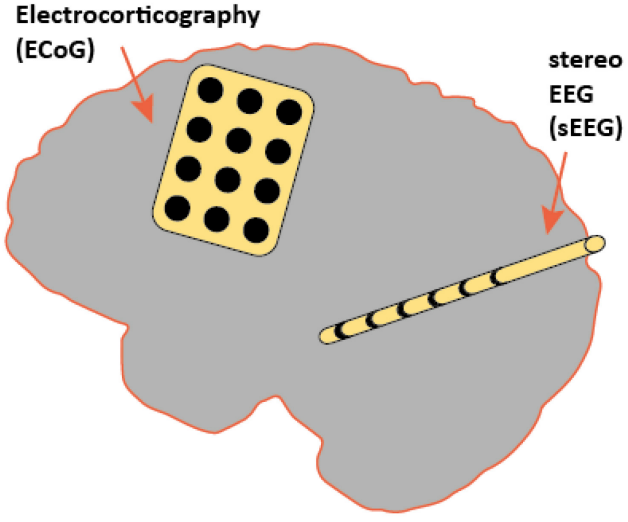

Figure 1.1: The two principal iEEG configurations ECoG and sEEG.

The interest of epilepsy surgery research is turning from delineating this localized EZ towards a network approach. In the network approach, epilepsy is caused by a collection of hyperexcitable nodes in an epileptogenic brain network that produces and propagates epileptic activity. Network disconnection of the connections that propagate epileptic activity could adapt the surgical strategy. Brain networks can be characterized with single pulse electrical stimulation (SPES) and diffusion weighted imaging (DWI).

1.2 Single pulse electrical stimulation

SPES is the delivery of electrical stimuli to adjacent electrode contacts that are part of an iEEG configuration, with such settings that only the neurons in the brain tissue directly near the electrode contacts are activated. The electrographic response to these stimuli could reveal connections between local and distant activated brain areas. Two types of electrographic responses are excited with SPES: physiological early responses (ER) and pathological delayed responses.

A typical ER consists of a spike often followed by a slow wave within 100 ms after the stimulus artifact (see Figure 1.2). This spike and slow wave are defined as the first and second negative deflections and are called the N1 and N2 peaks. Those peaks are alternated with positive deflections, the P1 and P2. The morphology of the ER and thus the presence and order of the P1, N1, P2, and N2 peaks is determined by the orientation of pyramidal cells relative to the stimulated and receiving electrode. The N1 peak describes direct cortical connections and the N2 peak demonstrates possibly also indirect connections [11], [12]. Brain networks characterized by SPES are named effective networks because they describe causal interactions between brain areas caused by perturbation of the brain areas.
A disadvantage of effective networks is that they only sample a small part of the whole-brain network and are only available after an invasive surgical intervention.

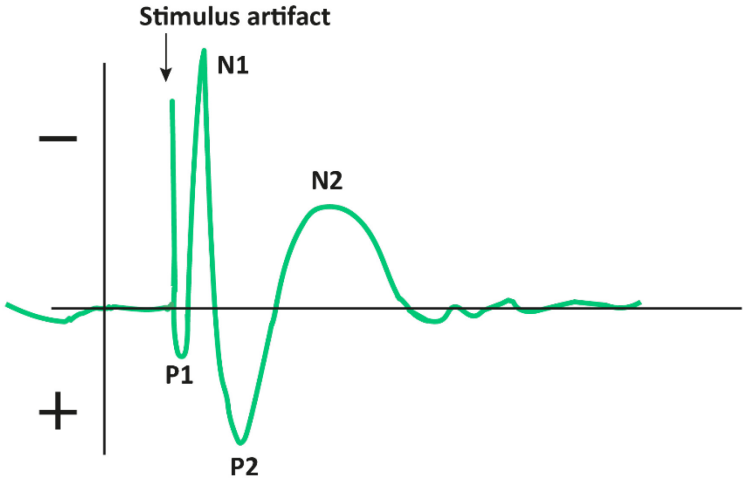

Figure 1.2: Typical electrographic response to single pulse electrical stimulation (SPES). The P1 peak is defined as the first positive peak, the N1 peak is the first negative peak, the P2 the second positive, and the N2 the second negative.

1.3 Diffusion weighted imaging

DWI is a magnetic resonance imaging (MRI) technique that captures the anisotropic diffusion of water molecules along myelinated axons to estimate the spatial organization of the white matter [13]. With fiber tractography (FT), the specific paths of white matter tracts between brain areas can be non-invasively reconstructed, allowing the identification of anatomical connections [14].

1.3.1 Acquisition of DWI data

The principle behind diffusion imaging is the Brownian motion of water molecules. Brownian motion is the phenomenon that water molecules move with a heat-driven, random velocity and in a random direction unless the movement is constrained by barriers [15]. In the brain, the most important barriers are myelinated axonal membranes in the white matter [13]. The directional constraining of movement due to barriers is called anisotropic diffusion. MRI can be used to capture diffusion in the human brain due to the high density of water and the ability of the hydrogen protons in water to freely move. The MRI sequence used for DWI is the spin echo pulse sequence, which components are illustrated in Figure 1.3 [13].

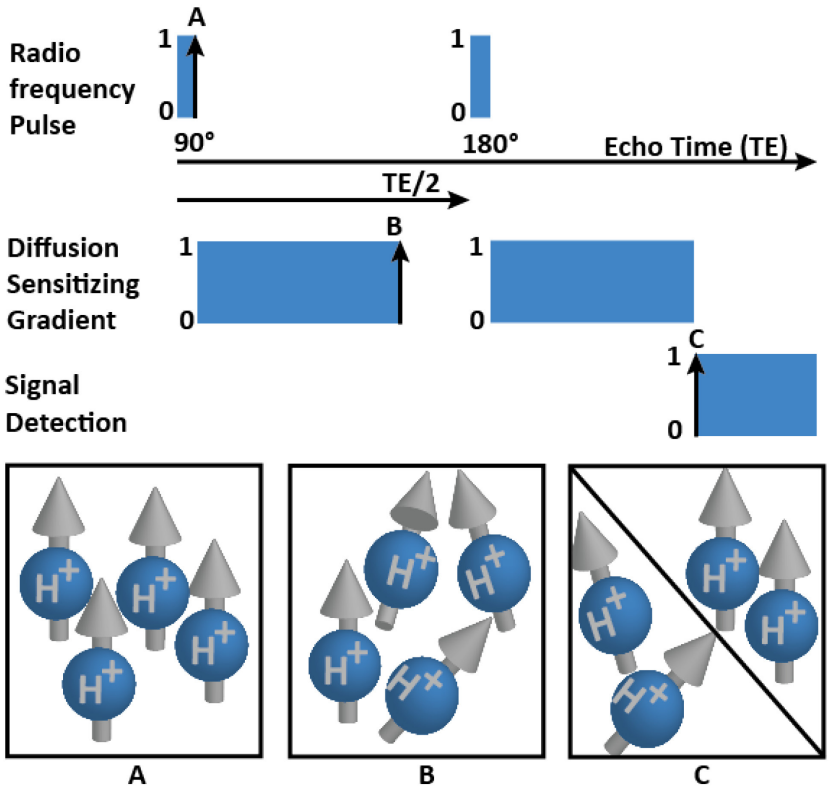

Figure 1.3: Graphical summary of the spin echo pulse sequence. A, B and C illustrate the hydrogen protons, in A) they have coherent phase, in B) divergent phase and in C) the phase depends on the diffusion.

The sequence starts with the excitation radiofrequency (RF) pulse of 90° which causes the hydrogen protons to have coherent phases (see Situation A, Figure 1.3). On top of the standard strong static magnetic field, a spatial gradient is activated to cause the hydrogen protons to develop divergent phases over time and space (see Situation B, Figure 1.3). This gradient is called the diffusion sensitizing gradient. To restore the initial phase coherence, halfway in the sequence an RF refocusing pulse of 180° is given and the diffusion sensitizing gradient is again activated. When there is no movement of water molecules, the diffusion sensitizing gradients cancel each other out and the refocusing pulse causes the protons to have coherent phases at the time of signal detection (see Situation C, Figure 1.3). The time between the excitation pulse and the signal detection is called the echo time (TE). If there is diffusion within the voxel during this TE period, the moved hydrogen protons do not experience the same magnetic field during the first and second half of the TE. This causes a loss of phase coherence and thus a weaker detected signal.

Using the spin echo pulse sequence, the average amount of diffusion D over time and space ($^{mm^2}/_{s}$) in one voxel can be calculated with

$$\frac{S}{S_0} = e^{-bD} \tag{1.1}$$

where, S and S_0 are the signal levels with and without the activation of the diffusion sensitizing gradient. D is the diffusion coefficient [16]. b is the value that indicates the strength of the diffusion sensitizing gradient, given by

$$b = \gamma^2 G^2 \delta^2 \left(\Delta - \frac{\delta}{3}\right) \tag{1.2}$$

with γ the gyromagnetic ratio of a hydrogen nucleus, G the size of the diffusion sensitizing gradient, δ the period of activation of this gradient, and Δ half of the TE period [16]. The b value determines the spatial sensitivity to diffusion. A regular DWI sequence with a b value of 1000 mm^2/s is sensitive to a water molecule displacement on a microscopic scale, which is approximately 2-18 µm in any direction [13]. A larger b value makes the DW images more sensitive to diffusion but decreases the signal-to-noise ratio due to the greater loss of phase coherence and thus a smaller signal of interest.

1.3.2 Fiber orientation distribution

Although DWI could provide interesting information about the microscopic diffusion properties of brain tissue, it does not take the directional constraints of diffusion into account [17].To be able to look at the directionality of diffusion, DWI images need to be made in different directions to reconstruct a diffusion coefficient along any arbitrary direction. This reconstruction is calculated by using a fiber orientation distribution (FOD), of which constrained spherical deconvolution (CSD) is the current best practice. The resolution of DWI that can be achieved, is in the range of mm's, which results in more than one fiber bundle in 90% of all white matter voxels [18]. The FOD describes the orientation and volume fractions of all these fiber bundles within a voxel. The volume fraction can be seen as a measure of diffusion strength. The more diffusion directions are acquired, the more precise the FOD model will be.

The CSD model requires two assumptions [19]. 1) The signals emanating from different fiber bundles are assumed independent from each other. Thus, the measured diffusion weighted signal attenuation S is the sum of all signals from the different fiber bundles present in the voxel. 2) The diffusion characteristics of these fiber bundles are assumed identical. In the CSD model, the signal from one fiber bundle is represented by a response function. The total signal $S(\theta, \emptyset)$ is the sum of these response functions, rotated such that they are aligned with their orientation and weighted by their volume fraction. This rotation is expressed in spherical coordinates with an elevation angle θ and an azimuthal angle ∅ (see Figure 1.4). This can be written in a formula as:

$$S(\theta, \emptyset) = \sum_i \hat{A}_i f_i R(\theta) \tag{1.3}$$

With $\hat{A}_i$ representing a rotation onto the direction $(\theta_i, \emptyset_i)$, f_i the volume fraction of the ith fiber bundle and $R(\theta)$ the response function.

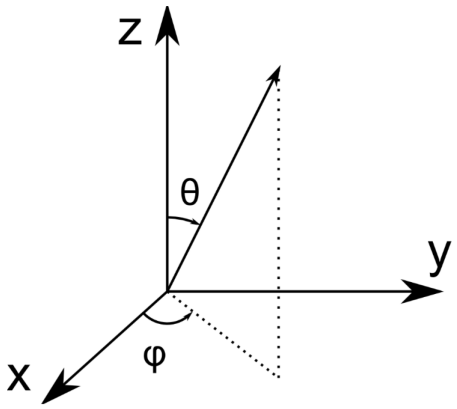

Figure 1.4: The spherical coordinate system with elevation angle θ and azimuthal angle ∅ [20].

Equation 1.3 can be expressed as the convolution over the unit sphere of the response function $R(\theta)$:

$$S(\theta,\emptyset) = F(\theta,\emptyset) \otimes R(\theta). \quad (1.4)$$

The FOD function $F(\theta,\emptyset)$ contains information about the directions $(\theta,\emptyset)$ with the highest volume fraction and is thus the characteristic you want to estimate to enable fiber tracking (section 1.3.3). Since we measure the signal $S(\theta,\emptyset)$and the response function $R(\theta)$ could be estimated, the $F(\theta,\emptyset)$ can be acquired with spherical deconvolution. The response function is estimated from the patient's DWI data by measuring the signal S in voxels likely to contain only one fiber bundle. Spherical deconvolution could be performed using spherical and rotational harmonics. These harmonics form an orthonormal basis set of functions over a sphere similar to the Fourier series. A spherical harmonics (see Figure 1.5) consists of a harmonic order n $(n \geq 0)$ and a phase factor m $(-n \leq m \leq n)$. The rotational harmonic has a harmonic order n $(n \geq 0)$ and two phase factors m and l $(-n \leq m, l \leq n)$. The nth order spherical harmonic decomposition of the signal $S(\theta,\emptyset)$ is given by the matrix multiplication:

$$\overrightarrow{S^n} = \boldsymbol{R}^n \overrightarrow{F^n}. \quad (1.5)$$

With $\boldsymbol{R}^n$ a matrix of size $(2n+1)(2n+1)$ and $\overrightarrow{F^n}$ a vector of length $(2n+1)$. Each $\boldsymbol{R}^n$ matrix must be inverted to calculate the $\overrightarrow{F^n}$ and finally get the FOD. The FOD needs to be constrained for negative values since those are physically impossible [21].

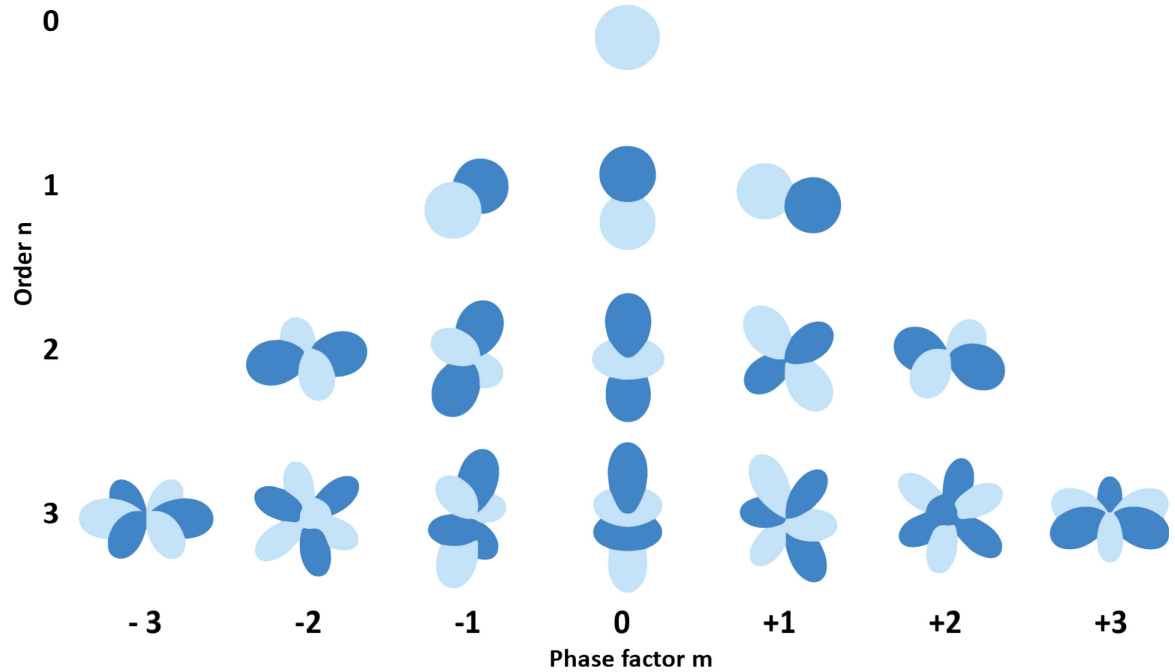

Figure 1.5: Visual representation of spherical harmonics orthonormal basis set of functions over the sphere up to order n = 3 (vertical) and phase factor m = [-n, +n] = [-3, +3](horizontal). This basis set is similar to how the Fourier series forms an orthonormal basis for the Cartesian space.

The harmonic order is inversely related to the resolution and limited by the diffusion directions. The maximal harmonic order is eight for 45 diffusion directions and 10 for 66 directions. However, spherical deconvolution is more sensitive to noise when using higher harmonic orders. Therefore a trade-off must be made between resolution and the influence of noise.

1.3.3 Fiber tractography

The FOD is used to perform FT. There are two primary methods for FT, deterministic and probabilistic tractography. With deterministic tractography, curved three dimensional lines, called streamlines, are

made by following the principal direction of the FOD from voxel to voxel. The direction of this streamline is calculated at each voxel by numerically solving the differential equation (DE) of the form

$$\frac{d\boldsymbol{r}(s)}{ds} = \boldsymbol{v}_1\big(\boldsymbol{r}(s)\big),\ \boldsymbol{r}(0) = \boldsymbol{r}_0 \quad (10)$$

with $\boldsymbol{r}(s)$ the curve at position s and $\boldsymbol{v}_1$ the principal direction vector [22]. This streamline determination is termed seeding. In probabilistic tractography, the direction of a streamline is determined by probabilities of the principal direction of the FOD in a certain voxel. For each voxel, the direction of the streamline is sampled from a FOD volume fraction probability profile. All the streamlines are assembled to produce statistical estimates of the white matter pathways.

To seed streamlines that could realistically be white matter pathways, some rules for the propagation of the streamline could be set. Examples of parameters that can be used are the maximum curvature angle to avoid unrealistic sharp turns, the maximum and minimum length of the streamline, and the minimal FOD volume fraction [23]. Furthermore, the FT procedure could be anatomically constrained by defining regions for start, propagation, and termination of the streamlines [24].

The result of FT is a number of streamlines that can be presented in a three dimensional image, called a tractogram. Brain networks characterized by DWI are named structural networks. Structural networks can solve the disadvantage of effective networks as non-invasive, whole-brain structural network analysis is possible.

1.4 Brain networks

A network is a way of organizing a system that consists of similar parts that are connected with each other. A network consists of two elements: nodes and edges. In the case of SPES and DWI based networks, nodes represent the brain area near an electrode. Edges are the effective or structural connections between the brain areas. These edges could be determined in a binary manner, by describing only the presence or absence of a connection or in a weighted manner by also taking the connectivity strength between two nodes into account. An overall comparison between two networks could be made with the Jaccard index, which measures the overlap between two binary networks [25]. Networks could be further analyzed with graph analysis [26]. The degree and betweenness centrality are examples of network characteristics, depicted in Figure 1.6. The degree of a node is the number of edges that are connected to that node and reflects the importance of this node in the network. The betweenness centrality quantifies the number of times a node is part of the shortest path between two other nodes. This is calculated by computing all shortest paths between the nodes in the network and determining the fraction of shortest paths that pass through the node of interest. Nodes with a high betweenness centrality are crucial nodes in the network that connect multiple nodes.

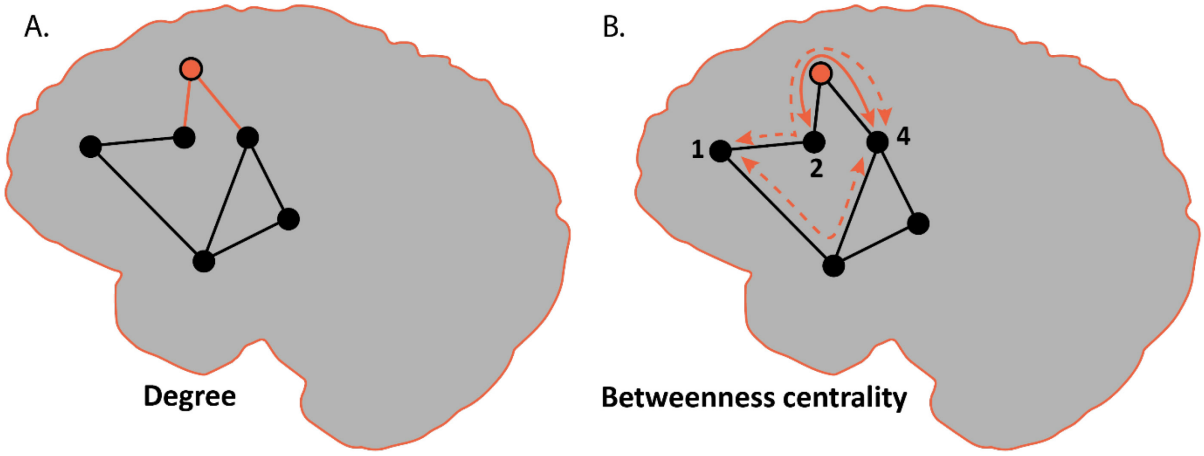

Figure 1.6: Graph measures in a network with 6 nodes and 7 edges. A) Degree. The orange node has a degree of 2. B) The betweenness centrality. The orange node is part of the shortest path between node 2 and 4. There are two possible shortest paths between node 1 and 4, of which the orange node is part of one of them. Therefore, the orange node has a betweenness centrality of 1.5.

1.5 Networks and epilepsy

The influence of epilepsy on the brain network organization is studied using both effective and structural networks. Studies using effective networks suggest that the epileptogenic tissue is densely interconnected. Van Blooijs et al. studied effective network alterations and reported a significantly higher degree of nodes within epileptogenic tissue compared to non-epileptogenic tissue [27]. They elucidated that this high degree was mainly caused by connections within the epileptogenic tissue. Boulogne et al. analyzed effective networks in a specific type of focal epilepsy caused by the structural pathology nodular heterotopia [28]. They characterized highly connected epileptogenic networks and showed that regions connected with pathogenic tissue are more likely part of the epileptogenic tissue. Studies using structural networks show that the network alterations caused by epilepsy might not be limited to the epileptogenic focus. Structural network studies reported a higher average shortest path length between nodes compared to controls, suggesting that the whole-brain structural networks in epilepsy patients are less efficiently organized [29]–[31]. Campos et al. observed structural network alterations in regions closely related to the presumed EZ [32]. Structural and effective network characterization describe seemly distinct influences of epilepsy on the network organization, thus might complement each other. The structural and effective network studies use different network characteristics and spatial scales, therefore is still unclear to what extent the structural and effective networks relate.

1.6 Objective

Other surgical strategies such as network disconnection are needed to further improve the success rate of epilepsy surgery. To reach that clinical goal, a better understanding of how epilepsy alters the patient-specific network is necessary. DWI in combination with SPES could deepen our understanding of epileptogenic networks by revealing the biologically plausible pathways that give rise to the observed effective connections between electrodes. We aimed to understand how structural and effective networks are related as a step towards clinical use of brain networks in epilepsy surgery. Therefore, we assessed the inter-modal similarity between non-invasive structural and invasive effective networks of focal epilepsy patients.'

1.7 Research questions

The aim of this research can be summarized by one main research question and two sub-questions.

- How do structural networks derived from DWI relate to effective networks obtained from SPES in patients with focal drug resistant epilepsy?
    a. What is the inter-modal similarity between structural networks derived from DWI and effective networks obtained from SPES?
    b. What is the influence of epilepsy on the correlation between network characteristics of structural and effective networks?

We hypothesize that structural and effective networks have a high inter-modal similarity when characterized on the same spatial scale. We expect that epilepsy decreases the correlation between network characteristics of structural and effective networks due to the seemly distinct network alterations reported.

To characterize effective networks, an automatic detector was optimized in Chapter 3. We developed an fiber tractography algorithm in Chapter 4 to characterize structural networks using DWI and determined structural connections between multiple intracranial EEG electrodes. In Chapter 5 we compared structural and effective networks and assessed the influence of epilepsy on their relation. The results of Chapter 5 were submitted for the European Epilepsy Conference in Geneva, 9-13 July 2022, and accepted for oral presentation (see Appendix A)

2. Optimization of automatic detection of early responses for stereo EEG

2.1 Introduction

Early responses (ER) evoked by SPES are physiological responses to stimulation of a local population of neurons and can reveal effective brain networks, as described in Chapter 1. Valentin et al. introduced the term 'early responses' in 2002 and defined it as a sharp deflection after the stimulus artifact followed by one or two slow waves of alternating polarity [33]. He and others identified ERs visually [34]–[37]. Annotating SPES is a time-consuming task since SPES performed in one patient results in around 3000 epochs. Automatic ER detection allows to investigate ERs and effective brain networks efficiently and objectively.

Several research groups developed automatic detectors to detect the occurrence, amplitude, and latency of ERs [8], [27], [38]. Van Blooijs et al. constructed and validated an automatic ER detector for ECoG data with a sensitivity of 78%, a specificity of 91%, a positive predictive value (PPV) of 75%, and a negative predictive value (NPV) of 92% [39]. This detector detects the occurrence of the N1 peak of the ER with the Matlab function peakfinder. The peakfinder is based on the standard deviation (SD) of the spontaneous background activity. Van Blooijs noted a significant ER when a positive N1 peak occurs within 9-100 ms after stimulation and the amplitude exceeds 2.6 times the SD of the baseline before stimulation. This detector cannot be used directly for sEEG data because of the morphological differences in ERs between the two iEEG configurations.

ERs from ECoG data have consistent morphologies with a negative first deflection (N1 peak) (see Chapter 1). In sEEG, the position of the stimulated and receiving electrode contact relative to the orientation of the pyramidal cells varies, which results in variation in the morphology of the ER [40]. The polarity of the stimulus artifact determines the polarity of the main deflection, a negative stimulus artifact results in the main deflection being the P1 peak (see Figure 2.1). Furthermore, we hypothesize that the amplitude of the main deflection (N1 or P1 peak) is different due to shorter interelectrode contact distance and lower stimulation currents. Shorter interelectrode contact distances increase the amplitude while lower stimulation currents decrease the amplitude but to what extent is not known. Therefore, the present SD threshold of 2.6 must be revised. Next to the SD threshold, two more settings are important for the functioning of the detector (see Figure 2.1). The minimal SD is set to prevent the detection of small peaks in signals with low voltage activity. The *sel*, defined as the voltage difference between neighboring time points to qualify as a peak, is set to prevent the detection of small peaks in signals with a slow trend after the stimulation artifact.

We adapted the automatic detector validated by van Blooijs to detect the occurrence of ERs in sEEG data [39]. The intention of the automatic detector is to sensitively detect ERs, after which the detected ERs are visually checked. The detector must be sensitive to make sure that most of the ERs are detected, while the number of false positive detections must be limited. We aimed to optimize the parameters of the automatic ER detector and validate the results for sEEG data to use the detector for the construction of effective networks.

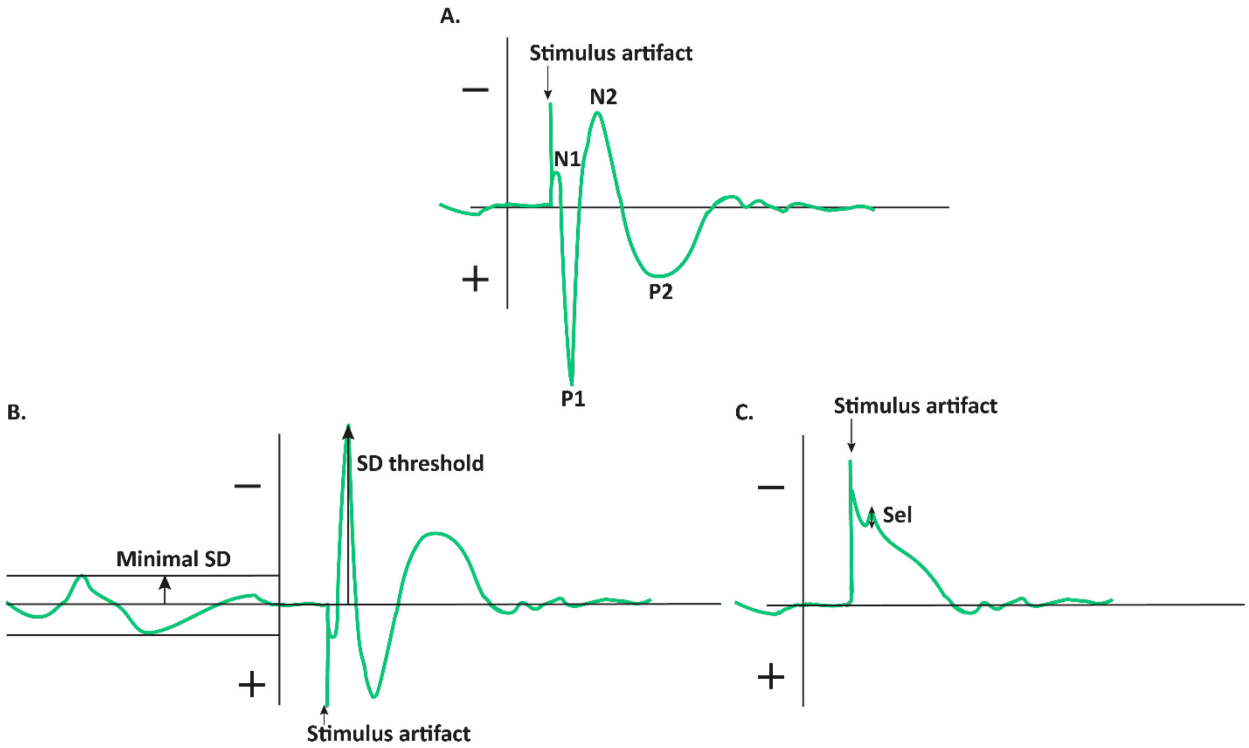

Figure 2.1: Important ER characteristics for the functioning of the ER detector for sEEG data. A) Example of an ER with a variation in morphology compared to ERs from ECoG data. B) The SD threshold is defined as the minimal ratio between the amplitude of the N1 peak and the SD of the baseline. When the SD of the baseline does not exceed the minimal SD, the minimal SD is used. C) Example of a slow trend after the stimulation artifact where the parameter sel prevents detection of small peaks.

2.2 Methods

2.2.1 Patient specification

We selected data from six patients who underwent SPES as part of an iEEG monitoring period with depth electrodes between 2014 and 2021. To ensure an independent patient subset from the patients selected in Chapter 4 and Chapter 5, the exclusion criterion was the presence of a diffusion weighted MRI. The patients were randomly divided into a training (50%) and validation (50%) subset. The clinical data were extracted from the RESPect database that consists of iEEG data from epilepsy surgery candidates treated at the University Medical Center Utrecht, the Netherlands [57]. iEEG data were recorded at 2048 Hz with a MicroMed LTM64/128 express EEG headbox with an integrated programmable stimulator (MicroMed, Mogliano—Veneto, Italy). The SPES stimulation protocol consisted of trials of ten monophasic stimuli applied to each pair of adjacent electrode contacts with a pulse width of 1 ms, a current of 1-4mA, and a repetition rate of 0.2 Hz. In three patients, we switched the cathode and anode after 5 stimuli. Only electrodes placed in the grey matter were stimulated.

2.2.2 Visual annotation

ERs were annotated by two observers (SJ and DvB) using in-house developed software with MATLAB (version R2021b, The Mathworks Inc., Natick, Massachusetts). Per electrode contact, we selected epochs with a time window of 2s pre- and 2 s post-stimulation. We averaged the ten epochs and subtracted the median amplitude of the averaged epoch during 2s pre-stimulation. We re-referenced the averaged epoch by subtracting the median epoch of the 5% signals with the lowest variance. The obtained post-stimulus signal where we expect the ERs is called the evoked response potential (ERP). We visually annotated the ERPs by plotting them per electrode contact and stimulus pair (see Figure 2.2).

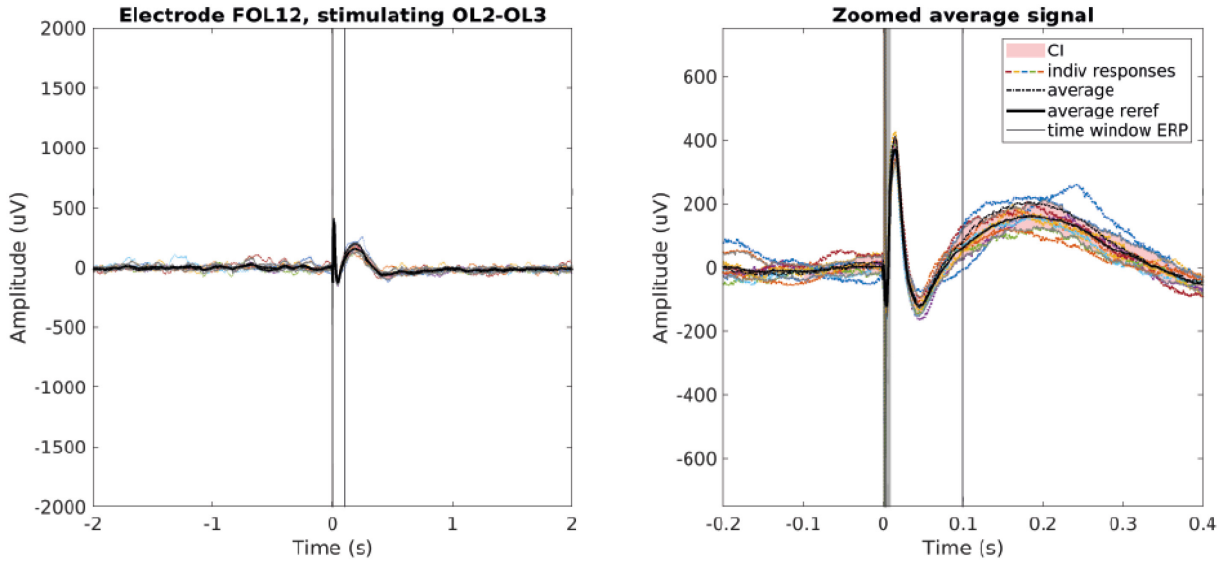

Figure 2.2: Example of an epoch with a plotted evoked response potential (ERP) of one electrode contact and stimulation pair. The individual signals (colors), averaged signals (dotted black) with confidence interval (CI, red marked), and re-referenced signals (black) were plotted in two time windows. Based on this plot, the ERs were annotated.

We determined the inter-observer agreement between the two observers with the unweighted Cohens kappa score. Common distinctive ERPs with no agreement were discussed between the two observers. Hereafter, all EPRs with no agreement were rescored by SJ and only ERPs where agreement is gained were annotated as ERs. We only included patients with a kappa score higher than 0.6 [41].

2.2.3 Optimization

The parameters SD threshold, *sel*, and minimal SD were varied to find the optimal combination for sEEG data. The SD threshold was varied between 0.5 and 15 with steps of 0.5. The *sel* was varied between 0 and 200 µV with steps of 10. The minimal SD of the baseline was varied between 0 and 100 with steps of 10. The baseline SD was calculated over the pre-stimulus period of 2 s. For each parameter combination, detector detected ERs with a P1 or N1 peak in the post-stimulus interval between 9 and 100 ms. Both P1 and N1 peaks that meet the, by the parameters defined criteria, were detected as ER.

The results of the detector were compared to the visual annotations and the ERPs were categorized as true positives, true negatives, false positives and false negatives. The sensitivity, specificity, positive predictive value (PPV), negative predictive value (NPV), false positive percentage (FPP), and false negative percentage (FNP) were calculated as

$$\text{Sensitivity} = \frac{\text{True Positive } (TP)}{TP + \text{False Negative } (FN)}, \tag{3.1}$$

$$\text{Specificity} = \frac{\text{True Negative } (TN)}{TN + \text{False Positive } (FP)}, \tag{3.2}$$

$$PPV = \frac{TP}{TP+FP}, \tag{3.3}$$

$$NPV = \frac{TN}{TN+FN}. \tag{3.4}$$

$$FPP = \frac{FP}{TP+TN+FP+FN}, \tag{3.5}$$

$$FNP = \frac{FN}{TP+TN+FP+FN} \tag{3.6}$$

The parameter combination resulting in the optimal detector performance was defined as the combination with the lowest distance to the upper-left corner of the ROC curve (d-ROC). The d-ROC was calculated as

$$d - ROC = \sqrt{(1 - \text{sensitivity})^2 + (1 - \text{specificity})^2}. \quad (3.7)$$

The d-ROC was used as the optimal performance metric because it was the most relevant parameter to acquire a high sensitivity and maintain a feasible amount of false positives [42]. The initial optimal parameter combination was used to adjust the parameter ranges and reduce the step size. We reduced the step size to 0.1 with a range of 2 around the initial optimal parameter value for the SD threshold. The step size was reduced to 1 with a range of 20 around the initial optimal parameter value for the *sel* and minimal SD. The detector ran again with these new parameter combinations, results were again compared with visual results, and the parameter combination with the lowest d-ROC was used for validation.

2.2.4 Validation

The detector with the parameter combination resulting in the lowest d-ROC was validated with the patients in the validation subset. Sensitivity, specificity, NPV, and PPV were calculated. A detector with a sensitivity of more than 80% and a PPV of more than 50% was considered reasonable for usage as ER detector for sEEG data with a visual check. A detector with a sensitivity of more than 80% and a PPV of more than 80% was considered reasonable for usage as ER detector for sEEG data without a visual check.

2.2.5 Benefit detector

We intended to save time by reducing the amount of ERPs that need to be visually checked. If a visual check was necessary, the percentage ERPs needed to be visually checked is calculated as

$$\%\ \text{ERPs to visually check} = \frac{TP+FP}{TP+TN+FP+FN} \quad (3.8)$$

2.3 Results

2.3.1 Patient specification

We included six patients (see Table 2.1). The three patients in the train set had a mean age of 33 ± 10 (mean ± standard deviation (SD)), the sEEG contained 52 ± 7 electrode contacts in the grey matter, and 41 ± 7 stimulus trials were applied. The validation subset contained three patients with a mean age of 21 ± 9), 43 ± 5 grey matter contacts, and 34 ± 4 stimulus trials.

Table 2.1: Patient specification. The kappa score of the validation subset is lower compared to the train subset. ; T= train; V= validation m = male; f = female; F = frontal; T = temporal; P = parietal; C = central; IH = interhemispheric; A = amygdala; H = hippocampus; I = insula; N= no; Y = yes

Patient	Train/ validation subset	Gender	Age at sEEG	Electrodes in grey matter (all electrodes)	Stimuli trials	Switched cathode & anode?	Visual ERs	Kappa score
1	T	f	19	58 (64)	50	N	1073	0.87
2	T	m	41	43 (75)	32	Y	149	0.90
3	T	f	38	56 (93)	40	Y	374	0.91
4	V	m	10	35 (74)	28	N	144	0.86
5	V	f	20	46 (70)	38	N	220	0.80
6	V	f	32	45 (82)	36	Y	318	0.78

2.3.2 Visual annotation

For the train subset, 1596 ERs were annotated of which 1073 were acquired in one patient. The validation subset consisted of 682 ERs. The inter-observer agreement was 0.89 ± 0.019 (mean ± SD) in the train subset and 0.81 ± 0.034 in the validation subset.

2.3.3 Optimization

The initial optimal parameter combination had an SD threshold of 4, a *sel* of 10 µV, and a minimal SD of 10. The adjusted parameter ranges were between 3 and 5 for the SD threshold, between 0 and 20 µV, and between 0 and 20 for the minimal SD. The parameter combination with the lowest d-ROC of 15 had an SD threshold of 3.5, a *sel* of 0 µV, and a minimal SD of 16 (see Figure 2.3). The detector with the lowest d-ROC in the train subset had a mean sensitivity of 89%, a mean specificity of 90%, a mean PPV of 78%, and a mean NPV of 96% (see Table 2.2). This performance resulted in an overall FPP of 7% and a FNP of 3% (see Figure 2.4 and 2.5).

Table 2.2: The performance of the detector in the train subset.

Patient	**Sensitivity (%)**	**Specificity (%)**	**PPV (%)**	**NPV (%)**	**d-roc**
1	92	82	80	93	20
2	83	96	70	98	17
3	83	94	74	96	18

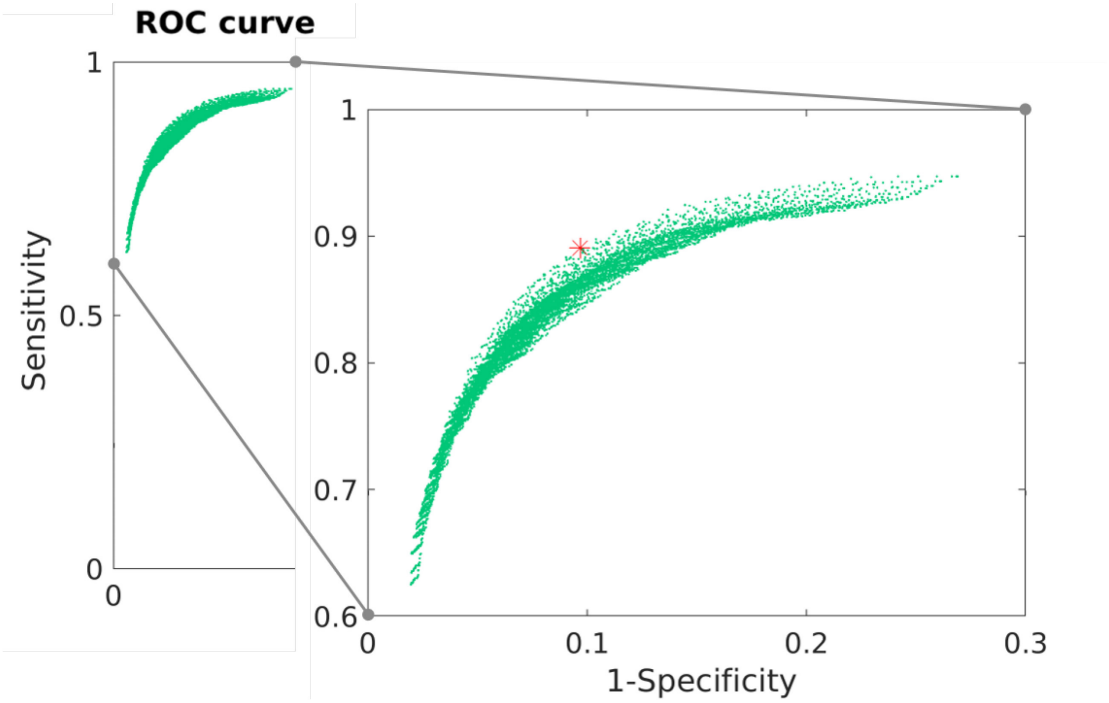

Figure 2.3: The ROC curve for the optimization with the adjusted parameter ranges. Each green dot represents the sensitivity and specificity of one parameter combination. The performance of the parameter combination SD threshold of 3.5, a sel of 0 µV, and a minimal SD of 16, chosen as best, is indicated with a red asterisk.

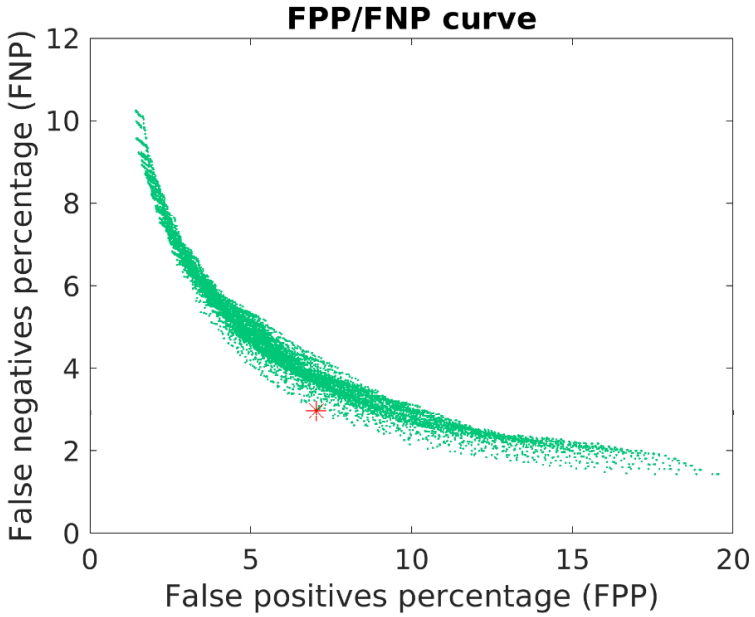

Figure 2.4: In this curve, the false positive percentage is plotted against the false negative percentage to get an indication of how they relate. The performance of the parameter combination SD threshold of 3.5, a sel of 0 µV, and a minimal SD of 16, chosen as best, is indicated with a red asterisk. We observed that the curve flattens to the right of this astrix and a small decrease in the false negatives results in a lot of false positives that need to be visually checked.

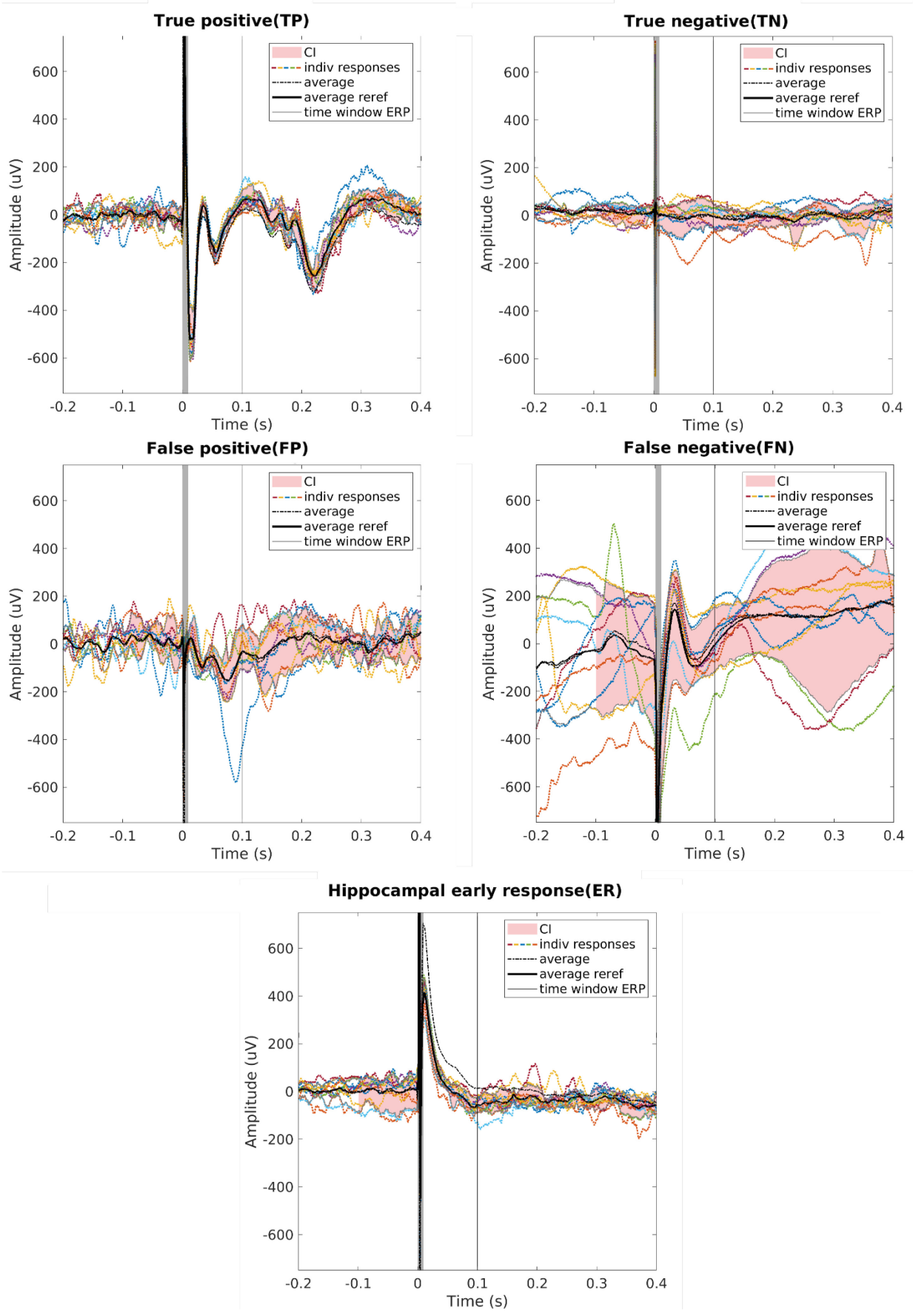

Figure 2.5: An example of a true positive, true negative, false positive, false negative, and distinctive hippocampal ER. The false positive ERP is an artifact. In the false negative ERP, the standard deviation of the baseline is large, which explains why the ER is not detected. The hippocampal ER is characterized by a short latency and a sharp peak.

2.3.4 Validation

The detector in the validation subset had a sensitivity of more than 80% (81%) and a mean PPV of more than 50% (75%) (see Table 2.3), thus was considered reasonable for usage as ER detector for sEEG data with a visual check. The mean specificity and mean NPV were respectively 93% and 96%.

Table 2.3: The performance of the detector in the validation subset

Patient	Sensitivity (%)	Specificity (%)	PPV (%)	NPV (%)
4	87	92	66	97
5	61	93	55	95
6	86	94	76	97

2.4 Discussion

We aimed to optimize the parameters of the automatic ER detector by Van Blooijs et al. for sEEG data and validate this optimized detector [39]. The optimized detector reliably detected ERs in sEEG data with reasonable sensitivity and a fair amount of false positives. A visual check of the detected ERPs is still necessary but, the amount of ERPs to check visually is reduced to 19% of the data, which saves a considerable amount of time.

The detector with the best performance had an SD threshold of 3.5, a *sel* of 0 µV, and a minimal SD of 16. We hypothesized that the amplitude of the second deflection of the ER was different in SPES in sEEG data compared to ECoG. The SD threshold was higher, from 2.6 to 3.5 for respectively ECoG and sEEG data. The minimal SD was set lower from 50 to 16 and we noticed that the mean SD of the sEEG baseline was lower than the SD of the ECoG baseline. Therefore we can conclude that the sEEG detector is more sensitive to lower amplitudes than the ECoG detector. The performance of the sEEG and ECoG detector are comparable with a sensitivity of 78% (ECoG) versus 81% (sEEG), a specificity of 91% versus 93%, a PPV of 75% versus 68%, and a NPV of 92% vs 96% [39]. Trebaul et al. also used the baseline before stimulation to determine the signal-to-noise ratio for the detection of ERs [43]. They reported a similar sensitivity of 86% when using the same amount of stimuli per trial. They generated surrogate data extracted from the baseline to calculate the significance threshold on the amplitude. This threshold could thus be expressed in a p-value (0.001) or z-score (5), which is hard to compare with our SD ratio.

The parameter *sel* had a value of 0 µV and thus did not have a function in the final detector. The parameter *sel* was originally included to account for the false positive detections caused by a slow trend after the stimulation artifact (see Figure 2.5). Including *sel* did not result in higher performances in this study. A reason for this may be that we wanted a sensitive detector and the parameter *sel* can also cause false negatives.

We used a common average reference montage including only channels with low variance. Other studies used a bipolar montage between adjacent electrode contacts within the same electrode to improve sensitivity to local current generators [8], [44]. Mitsuhashi et al. studied the effect of sEEG montage on the occurrence of ERs [44]. They concluded that ERs detected with a bipolar montage reflect solely near-field potentials from the cortex near the electrode contact, while ERs detected with an average montage could also be generated by a distant source. Practically, a stimulus pair that evoked an ER in many electrode contacts may be present in the average signal and thus in every electrode contact signal. The disadvantage of a bipolar montage is that we could not determine which of the electrode contacts is responsible for the detected ER. Therefore a combinational use between the average and bipolar montage may be a beneficial improvement to characterize brain networks with SPES for sEEG more reliable.

2.4.1 Strengths and limitations

A strong point of this study is that the visual annotation was performed by two observers. The inter-observer agreement in both the train and validation subset was >0.78 which is considered high [45]. The inter-observer agreement was 0.08 lower in the validation subset, which may be explained by the time sequence of scoring. The two observers reached a consensus about the scoring at front and started annotating with the train subset. Although the inter-observer agreement was high, we discovered some common distinctive ERs we were not familiar with in ECoG data. This resulted in an inconsistent scoring of these distinctive ERs. Therefore, a rescoring is done after a consensus was reached about the distinctive ERs. An example of a distinctive ER is an ER evoked in the hippocampal electrode contacts characterized by a short latency and a sharp peak (see Figure 2.5).
A limitation of this study is that we did not evaluate the performance of the detector on distinctive ERs between distinct anatomical areas. Frauscher et al. made an atlas of the normal sEEG signal and concluded that the sEEG signal and amplitude can largely differ between cortical areas [46]. This could lead to a lower performance of the detector in areas with a lower ER amplitude and must be accounted for in further research. Furthermore, the SPES protocol differed between patients, in half of the patients we switched the cathode and anode after 5 stimuli. The SPES protocol was updated at a certain moment and this switch was introduced to facilitate discarding the stimulation artifact. We included patients stimulated with both SPES protocols in this study because we wanted this detector to be applicable for both SPES protocols. Lastly, a large part of the ERs were annotated in one patient in the train subset which may indicate that this patient had a large influence on the parameter optimization.

2.4.2 Future perspectives

Ideally, we want to use the ER detector fully automatically without visually checking the detected ERs. To reach this goal, both the number of false positive detections and the number of false negative detections must be improved. Ideally both the FPP and FNP (see Figure 2.4) are close to 1%. To decrease the number of FP detections, the non-stimulation triggered events, such as interictal epileptic discharges or artifacts, must be removed. This could be done by excluding individual ERPs in epochs that exceed the median ERP over the whole epoch [43]. To increase the sensitivity, the artifact removal can be further improved so that we do not miss ERs hidden in a noisy signal. An improvement to the SPES protocol could be to add more stimuli to one trial. According to David et al., who constructed the first version of the detector improved by Trebaul et al., 40 stimuli per trial already resulted in sensitivities approaching 100% [8] [43]. In the current clinical workflow, this is not a feasible solution since the time to perform the SPES stimulation will be four times as high, while the current SPES stimulation protocol already takes an hour.

Lastly, we focused on optimizing the detector to detect the occurrence of an ER. The detector for ECoG is also able to detect the amplitude and latency of the N1 peak of the ER. This is relevant for quantifying effective connectivity and can be a subject for further study.

2.4.3 Conclusion

We optimized the automatic ER detector by Van Blooijs et al. for stereo electroencephalography (sEEG) data [39]. The sensitivity, specificity, PPV and NPV of this validated detector were respectively 81%, 93%, 68%, and 96%. We conclude that the optimized ER detector presented in this chapter can be used for the characterization of effective networks. In the next chapter, we constructed a fiber tractography algorithm for the characterization of structural networks.

3. Development of an invasive EEG constrained fiber tractography algorithm

3.1 Introduction

Fiber tractography (FT), derived from diffusion weighted imaging (DWI), is a technique that estimates the white matter tracts between brain areas and allows the reconstruction of structural brain networks, as described in Chapter 1. Basser et al. were the first to successfully perform in vivo FT in 2000 [22]. Nowadays, FT is clinically used to delineate large fiber tracts for pre-surgical planning and intra-operative navigation in neurosurgery [24]. In neuroscience research, FT is often used to non-invasively reconstruct a structural brain network of the whole-brain [47]. Because focal epilepsy is regarded as a network disease with epilepsy-related structural abnormalities, reconstruction of structural networks could be beneficial to understand which part of the epileptogenic network is diseased. To assess the feasibility of FT to characterize epileptogenic networks, our goal is to compare networks based on FT with the already clinically used effective networks derived from SPES (see Chapter 2). An FT algorithm based on invasive electroencephalography (iEEG) locations allows investigation of the relation between structural and effective networks.

Multiple research groups performed FT based on intracranial electrodes [14], [25], [38], [48]–[54]. They used either basic deterministic methods, such as the streamline tracking technique algorithm (STT) and the second-order Runge Kutta, or the more advanced iFOD2 algorithm (see Table 3.1). The iFOD2 algorithm is a probabilistic FT algorithm that performs second-order integration over the fiber orientation distributions (FOD) [55]. FOD volume fraction probability profiles are made using trilinear interpolation. The iFOD2 algorithm has six crucial algorithm parameters that affect the performance of the FT algorithm: the FOD threshold, the path step size, the maximum curvature angle, the minimum and maximum streamline length, and the streamline density threshold. The FOD threshold determines the minimal volume fraction, thus diffusion strength, in a specific direction to allow tracking in that direction. With a lower FOD threshold, more noisy streamlines are tracked and a higher FOD threshold leads to fewer and more restricted streamlines [56]. The path step size determines how often the algorithm takes an independent sample from the FOD probability profile. A larger step size makes the streamlines smoother, while a smaller step size introduces more wobbly streamlines [56]. The optimal step size is the largest step size with sufficient accuracy due to the large computation time of small step sizes. The maximum curvature angle defines the angle that is allowed between steps. With a high angle, more spurious streamlines are tracked, but the angle must be high enough to track U-fibers with a sharp curvature. The minimum and maximum streamline lengths could be used to constrain biologically implausible short or long streamlines. The streamline density threshold determines the minimal amount of streamlines to form a structural connection. The ideal setting of these parameters depends on the intended application, quality of the DWI scan, and specific processing algorithms used beforehand.

In this chapter, we describe how we developed an iEEG constrained FT algorithm based on the iFOD2 algorithm. We intended to make an algorithm that is sensitive for tracking all plausible connections, including streamlines with a long distance or a large curvature. A second, inferior requirement was that the risk of tracking biologically implausible streamlines must be minimized. We aimed to construct an iEEG constrained FT and optimize its parameters to use the algorithm for the construction of structural networks.

Table 3.1: Summary of methods used for an iEEG constrained fiber tractography algorithm [14], [25], [38], [48]–[54].NS = not specified; ECoG = electrocorticography; sEEG = stereo-EEG; DBS = deep brain stimulation; STT = streamline tracking technique; iFOD2 = second order integration over fiber orientation distributions.

	ECoG/sEEG	Seed region	Probabilistic/ determinicstic	Tractography algorithm	Tractography toolbox	Path step size	Nr. fibers	Min/max streamline length	Maximum curvature treshold	FA/FOD treshold
Tertel et al. 2011	ECoG	NS	deterministic	STT	DTIQuery	1 mm	NS	NS/300 mm	45°	0.15
Conner et al. 2011	ECoG	20 x 20 x 20 mm cuboidal	deterministic	STT	DTIQuery	2 mm	NS	NS/300 mm	45 °	0.15
Swann et al. 2012	ECoG	1cm cuboids	deterministic	STT	DTIquery	1 mm	NS	5/300	45°	0.15
Silverstein et al. 2020	ECoG	4 mm sphere	probabilistic	iFOD2	MRTrix	NS	3000 seeds/voxel	20/250 mm	70 °	NS
Filipiak et al. 2021	ECoG	NS	probabilistic	iFOD2	DIPY	0.5 mm	5000 seeds/voxel	NS/500 mm	30°	0.25
O'Hara et al. 2022	ECoG	4 mm sphere	probablistic	iFOD2	Mrtrix	0.5 mm	1x108 / ROI	NS	35°	NS
Crocker et al. 2021	sEEG	1 cm sphere	NS	NS	Probtrackx2	NS	NS	NS	NS	NS
Mitsuhashi et al. 2021	sEEG	5 mm sphere	NS	NS	DSI studio	0.3 mm	NS	10/250 mm	70 °	0.2
Kaufmann et al. 2021	sEEG	5 mm sphere	deterministic	2nd order Runge Kutta	Trackvis	NS	NS	NS/200 mm	35°	0.1
Waters et al. 2018	DBS electrodes	NS	probablistic	NS	Fdt toolbox	0.5 mm	5000 seeds / voxel	NS/1000 mm	NS	0.2
Parker et al. 2018	ECoG + sEEG	5 mm sEEG, 10 mm ECoG	probabilistic	iFOD2	MRTrix	0.2 mm	100 seeds /voxel	NS	60 °	0.1

3.2 Methods

3.2.1 Patient specification

We selected data from four patients who underwent both a diffusion weighted MRI and long-term, intracranial EEG monitoring between 2018 and 2021. Inclusion criteria were the presence of a DW image, a T1-weighted MRI, and a post-implementation CT scan. The iEEG data were extracted from the RESPect database and the DWI data from the Brain Computer Interface group [57].

3.2.2 DWI acquisition

DWI was acquired using a multi slice, multi shot echo-planar imaging (EPI) sequence with TE = 91 ms, TR = 3191 ms, field of view (FOV) = 224 x 132 x 224, and resolution = 2 x 2 x 2 mm^3. 62 volumes with a $b_1$value of 1600 $^{s}/_{mm^2}$were obtained with as principal phased-encoded direction the Posterior-Anterior (PA) direction. One b_0 scan in both the Anterior-Posterior (AP) and PA direction was obtained**.** The total scan duration was 204.1 seconds. A 3D T1 MRI was obtained at the same time as the DWI for anatomical reference (MRI-DWI) and was acquired with a turbo field echo sequence with TE= 3.8 ms, TR = 8.4 ms, TI = 1150 ms, FOV = 288 x 288 x 175, and resolution = 1 x 1 x 1 mm^3. The MRI-DWI was de-skulled using the brain extraction tool (bet) from the FSL toolbox for visualization purposes. Another 3D T1 MRI (MRI-CT) was acquired pre-implementation with a turbo field echo sequence with TE= 3.04 ms, TR = 6.21 ms, FOV = 240 x 240 x 180, and resolution = 0.6 x 0.6 x 0.6 mm^3. The MRI-CT and post-implantation CT scan, with a resolution of 0.6 x 0.6 x 0.6 mm^3, were used to extract the intracranial electrode contact coordinates.

3.2.3 Pre-processing

All processing was performed with the MRtrix3 package and MATLAB version R2021b (The Mathworks Inc., Natick, Massachusetts), combined with the brain imaging toolboxes Freesurfer, FSL, ANTs, and SPM12 [58]. The DWI data were preprocessed to improve the signal-to-noise ratio (SNR) and correct for common distortions. Consecutively MP-PCA denoising, Gibbs ringing correction, Eddy current correction, EPI distortion correction, movement distortion correction, b_0 field inhomogeneity correction, and b_1 bias field correction was performed. We improved the SNR using Marchenko-Pastur Principal Component Analysis (MP-PCA). MP-PCA is based on identifying noise-only principal components, thus all anatomical information is retained [59]. We removed Gibbs ringing artifacts in the grey-white matter boundary with an algorithm based on modeling the artifact with the sinc-

function [60]. Geometric distortion due to the EPI sequence and movement distortions were corrected using the FSL TOP UP tool. The TOP UP tool uses b_0 data in the principal and reversed phase-encoded direction to model the geometric shearing per slice [61]. Eddy currents artifacts were removed by modeling the diffusion signal as a Gaussian Process and assuming that the two phase-encoded directions measure an identical signal [62]. The b_0 field inhomogeneity was corrected by calculating the mean for both phase-encoding directions. The b_1 bias field is the spatially biased signal intensity due to radiofrequency field inhomogeneities which affects the fiber orientation model. The b_1 bias field was estimated from the corrected b_0 data and applied to all b_1 volumes [63]. We inspected the quality of the preprocessing by visually checking the processed DWI data and residual data step for each patient and preprocessing step (see Figure 3.1).

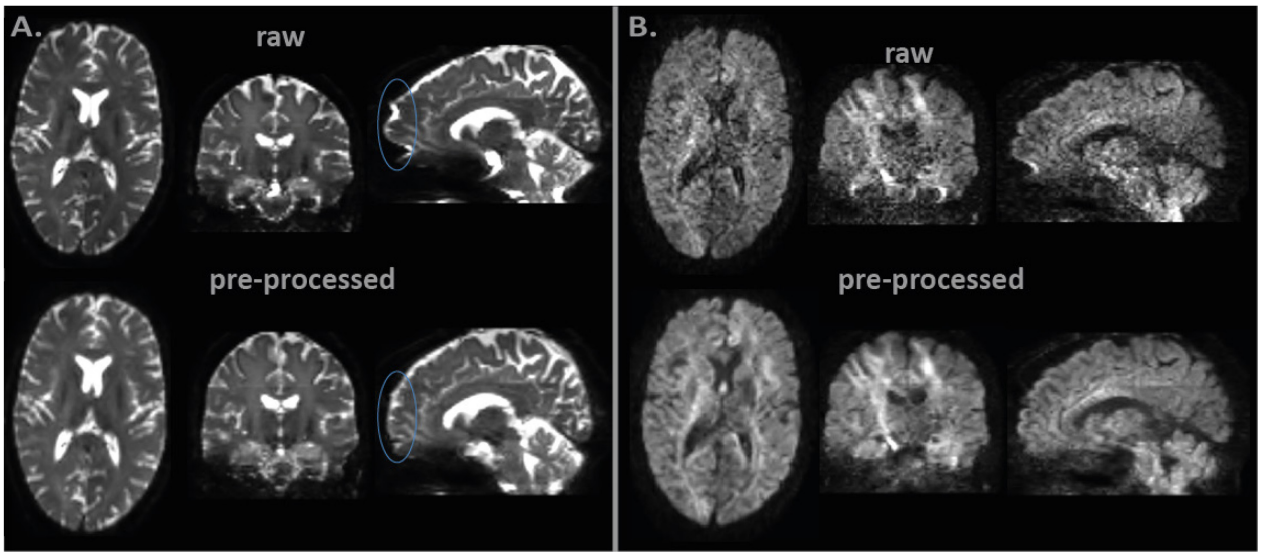

Figure 3.1: Raw and pre-processed images of a DWI volume. A) b_0 DWI volume. The geometric distortions are clearly improved as seen in the blue circles. B) b_1 DWI volume. The SNR is clearly improved.

3.2.4 Co-registration

The CT scan was linearly co-registered to the MRI-CT as the reference image, and the electrode contact coordinates were extracted from the CT scan. The MRI-DWI was linearly co-registered to the DWI b_0 image using the objective function normalized mutual information with the SPM toolbox. Normalized mutual information is the best objective function for images with a difference in contrast [55]. We used the MRI-DWI as the source image because the transformation of all 62 b_1 volumes is not beneficial for the data quality [64]. Lastly, the MRI-CT was linearly co-registered to the MRI-DWI as the reference image using the within-modality objective function normalized cross correlation with the SPM toolbox. Non-linear registration was not needed because we preprocessed the data and all the transformations were intra-subject. We segmented the MRI-DWI in six binary brain masks containing cortical grey matter, subcortical grey matter, white matter, the grey-white matter boundary, cerebrospinal fluid, and if present pathological tissue. We defined electrode contact areas in the grey-white matter boundary of the MRI-DWI, where the white matter pathways start, with a volume of 64 mm^3 to constrain the FT (see Figure 3.2). For each electrode contact coordinate, the 64 voxels in the grey-white matter boundary with the shortest Euclidian distance to the actual contact positions were the electrode contact areas. Overlapping voxels were assigned to the nearest electrode contact.

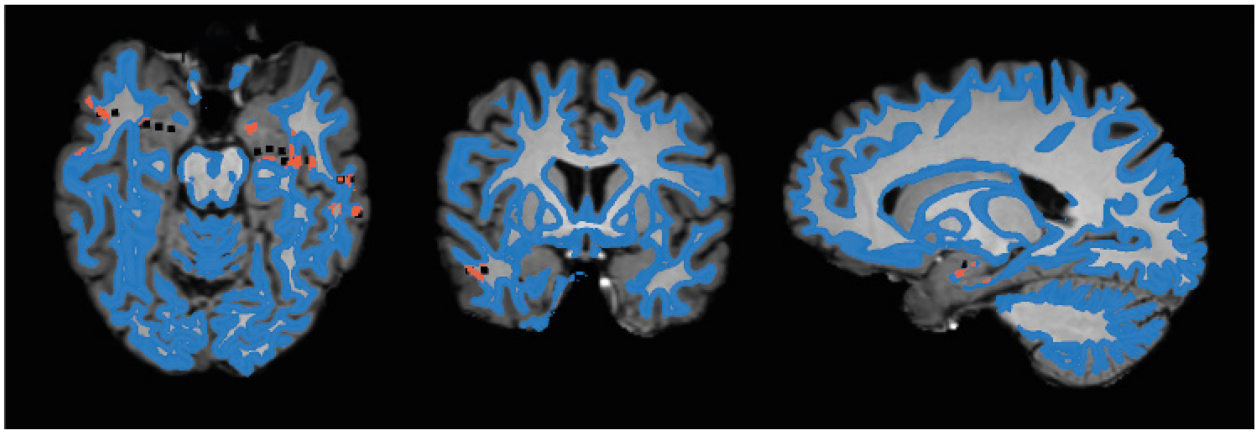

Figure 3.2: Electrode contact areas (orange) and the electrode contact coordinates (black) are displayed as an overlay on the MRI-DWI with the segmented grey-white matter boundary visualized in blue. We see that the electrode contact areas are located near the real electrode contact coordinates.

3.2.5 Fiber orientation model

We used Multi-Shell Multi-Tissue Constrained Spherical Deconvolution (MSMT-CSD) with a maximal harmonic order of eight to calculate the fiber orientation distributions (FOD). For each patient, the response function was estimated from the DWI data with the dHollander algorithm [14]. With two unique b values (b_0 and b_1), we could resolve FODs for two tissue types, white matter and non-white matter (see Figure 3.3).

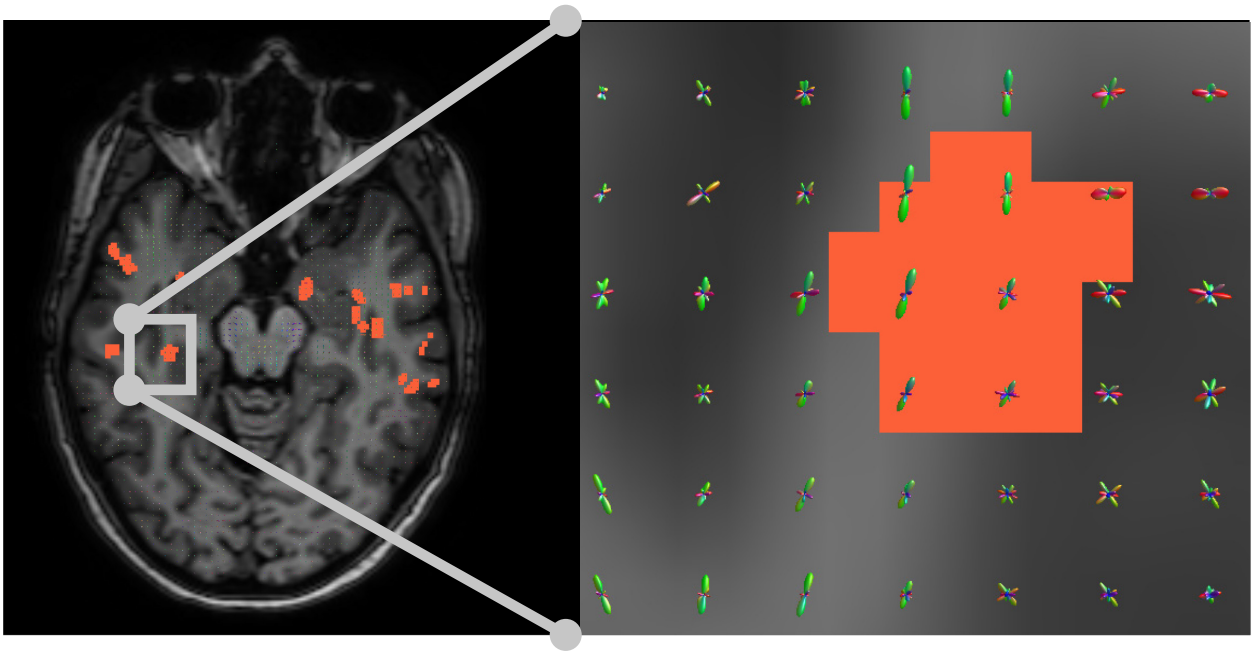

Figure 3.3: Fiber orientation distributions (FODs) displayed as an overlay on the MRI DWI. The electrode contact areas are displayed in orange. The shape of the FODs in and around the electrode contact area show that the area is located on the grey-white matter boundary. The grey matter is located on the left and upper right of the electrode contact area.

1.3.1 Parameter optimization

We performed anatomical constrained probabilistic tractography using the iFOD2 algorithm with a seed density of 6000 seeds per voxel. We optimized the parameters: FOD threshold, path step size, maximum curvature angle, minimum and maximum streamline length, and streamline density threshold of the algorithm by starting with a set of 'standard' parameter settings, which were the most common setting used in previous studies. The standard parameter setting, varied parameter

settings, and our strategy to optimize the parameters settings is summarized in Figure 3.4. We varied the maximum curvature angle separately for sEEG and ECoG patients to respectively 30° and 70°. For each setting, streamlines were created between all electrode contact areas. The streamline density was calculated by the number of streamlines divided by the volume of the two involved electrode contact areas. A structural connection was formed when the streamline density exceeds the streamline density threshold. All connections formed with a varied parameter setting were sorted on the absolute difference in streamline density between the standard and the varied parameter setting per patient. Two types of connections were defined: extended and restricted connections. An extended connection was a connection with a larger streamline density in the varied parameter setting compared to the standard setting. A restricted connection is defined as a connection with a smaller streamline density in the varied parameter setting compared to the standard setting. The first 5% of the connections with the largest difference in streamline density (either extended or reduced) between the two settings was visually inspected by SJ. If less than 10% of the connections to be visually annotated consisted of restricted or extended connections, we only visually annotated the respectively extended or restricted connections. The connections consisting of streamlines, the de-skulled MRI-DWI, and two electrode contact areas involved in the connection were shown. Each inspected connection was rated as plausible, if its streamlines showed reasonable paths, or spurious, when its streamlines showed an unlikely path. A parameter was deemed better than the standard parameter when the parameter variation resulted in more extended plausible connections than extended spurious and restricted plausible connections.

We calculated the network density of the structural networks d_{SC} as the number of actual formed structural connections divided by the number of potential connections:

$$d_{SC} = \frac{2*SC}{N(N-1)} \quad (3.1)$$

with SC the number of formed structural connections and N the number of electrode areas. The network density is used to determine if a reasonable amount of structural connections is characterized. Network densities between 6-17% are previously reported, and used as reference [24].

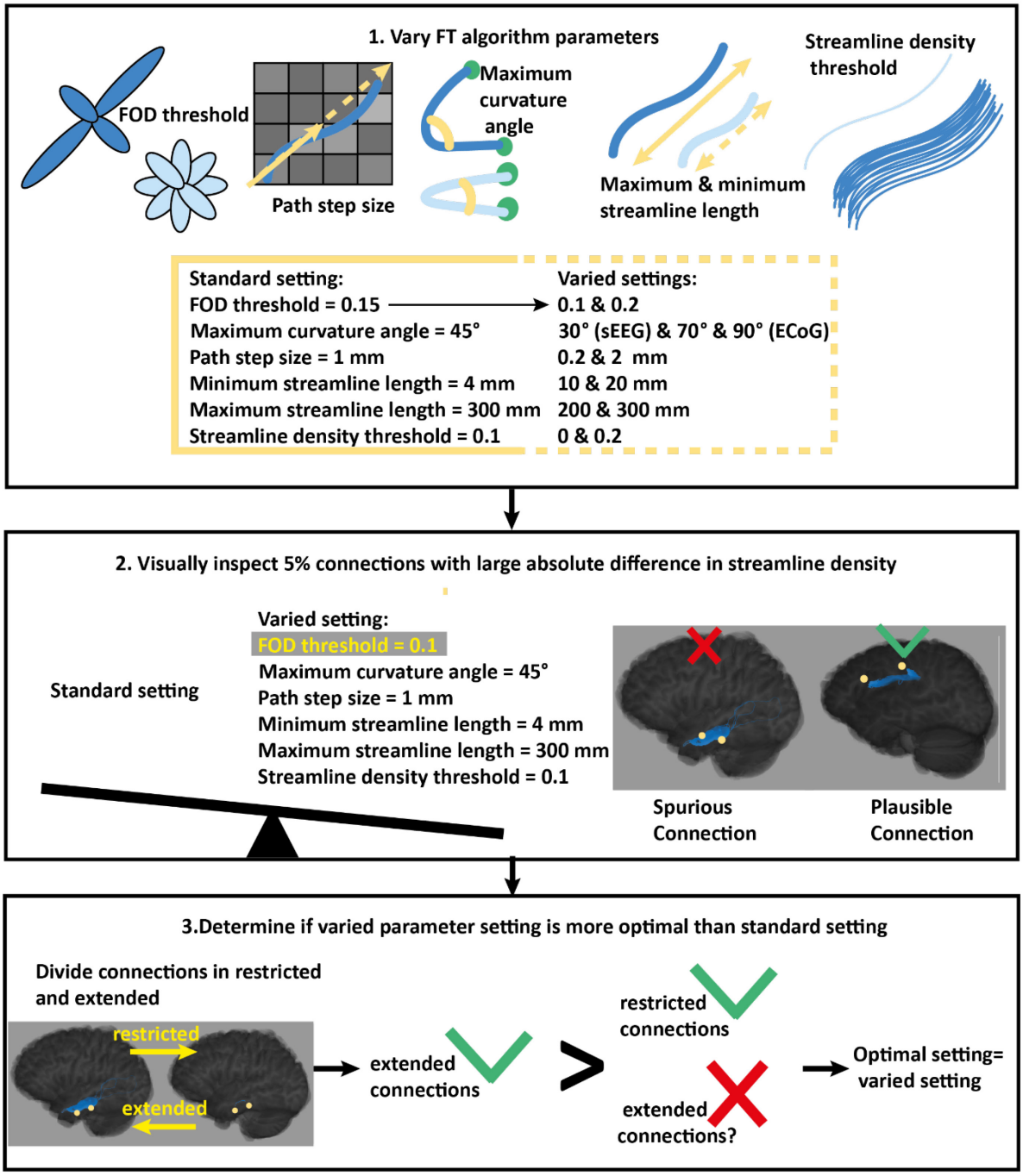

Figure 3.4: Strategy to optimize the parameters of the FT algorithm. 1. We varied each FT algortihm parameter separately and kept all other parameters the same as in the standard setting. 2. We visually inspected the first 5% of the connections sorted on the absolute difference in streamline density between the standard and the varied parameter setting. A connection was rated as plausible, if its streamlines showed reasonable paths, or spurious, when its streamlines showed an unlikely path. 3. The varied parameter setting was deemed more optimal when it resulted in more plausible connections than with the standard parameter setting and not too much new spurious connections were introduced. This requirement is formalized by defining the varied parameter setting as optimal setting when the number of extended plausible connections is larger than the number of restricted plausible connections and extended spurious connections.

3.3 Results

3.3.1 Patient specification

We included four patients with no or mild abnormal MRI (see Table 3.2). Two patients underwent sEEG and two patients underwent ECoG.

Table 3.2: Patient specification of the patients with ECoG (first 2 patients) and sEEG (last 2 patients). m = male; f = female; F = frontal; T = temporal; P = parietal; C = pre or post-central gyrus; IH = interhemispheric; A = amygdala; H = hippocampus; R=right; L=left; N = normal MRI; WA = white matter abnormalities; FCD = focal cortical dysplasia; mMCD = mild malformation of cortical development; NP=no pathology found.

Patient	ECoG/ sEEG	Age at iEEG	iEEG location	Sampled hemisphere	Included electrodes (all electrodes)	Electrodes in SOZ	Abnormal MRI	Pathology
1	ECoG	28	T	L	71 (72)	4	N	mMCD
2	ECoG	44	F,T,IH	L	71 (80)	15	WA	FCD type 2A
3	sEEG	50	F,T,A,H	R & L	47 (88)	4	Cysts	NP
4	sEEG	17	F,C,T,P	L	47 (89)	11	Possible FCD	mMCD

3.3.2 Parameter optimization

In total, 816 connections were visually annotated. The standard parameter setting resulted in a network density of 17% (range between patients: 6-23%) (see Figure 3.5). The varied maximum curvature angle of 70° and the maximum streamline length of 400 mm resulted in a higher percentage of extended plausible connection and were therefore deemed as better than the standard parameter settings (see Figure 3.6). The optimal algorithm parameters for sEEG and ECoG were a FOD threshold of 0.15, a maximum curvature angle of 70°, a minimum streamline length of 4 mm, a maximum curvature angle of 70°, a minimum streamline length of 4 mm, a maximum streamline length of 400 mm, and a streamline density threshold of 0.1.

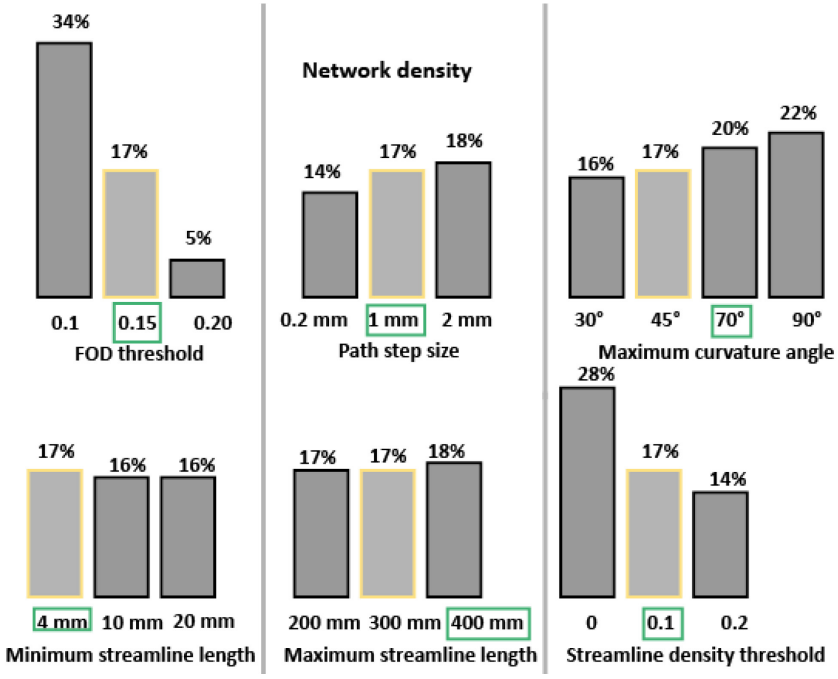

Figure 3.5: Varying the FOD threshold and streamline density threshold resulted in a large effect in the network density. The yellow bars indicate the standard setting. The optimal parameter setting is encircled in green.

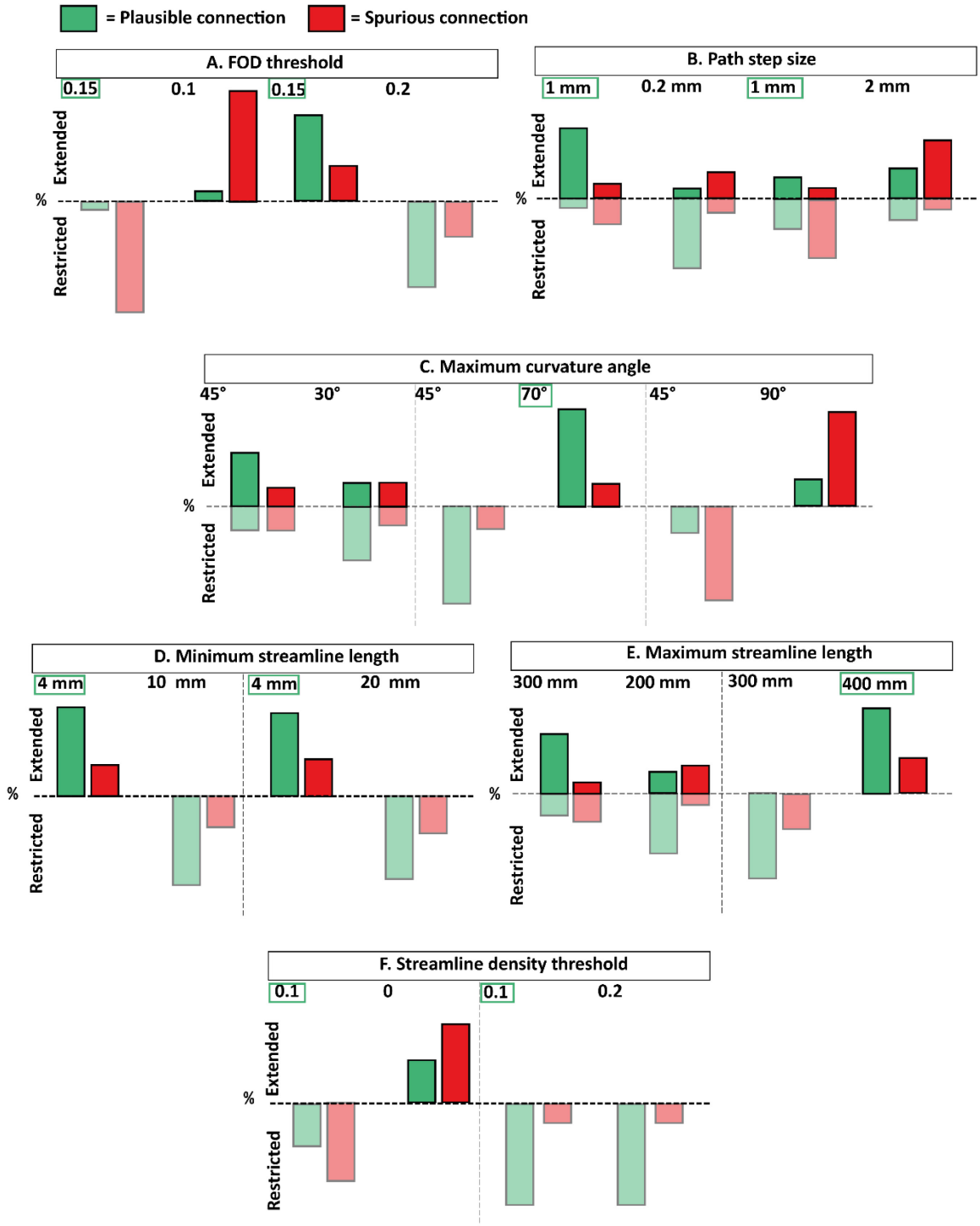

Figure 3.6:Overview of the parameter optimization where we visually inspected formed connections and compared them between the standard and varied parameter settings. Green bars indicate the percentage visually annotated plausible connections and red bars indicate the spurious connections. The transparent bars indicate the connections that are observed in the other parameter setting and are thus restricted in this setting. The optimal parameter setting is encircled in green. A) When we compare the FOD threshold of 0.15 with the varied setting of 0.1 we see that the number of extended plausible connections is much smaller than the number of extended spurious connections, thus the varied setting is not better than the standard setting (see Figure 3.4). For the comparison of a FOD threshold of 0.15 versus 0.2, we observe less extended plausible connections than restricted plausible connections. Thus we can conclude that a FOD threshold of 0.15 was the optimal setting. B) A path step size of 1 mm resulted in the most extended plausible and restricted spurious connections. C) With a maximum curvature angle of 70° the most plausible connections were extended. D) With a higher minimum streamline length, more plausible connections than spurious connections were restricted. E) A maximum streamline length

of 400 mm resulted in the most plausible connections being extended. F) A streamline density threshold of 0.1 resulted in more plausible connections than spurious connections extended and is thus deemed best.

Inspection of structural connections in each parameter setting showed that the optimal algorithm parameters resulted in the most plausible connections and the least spurious connections (see Figure 3.7).

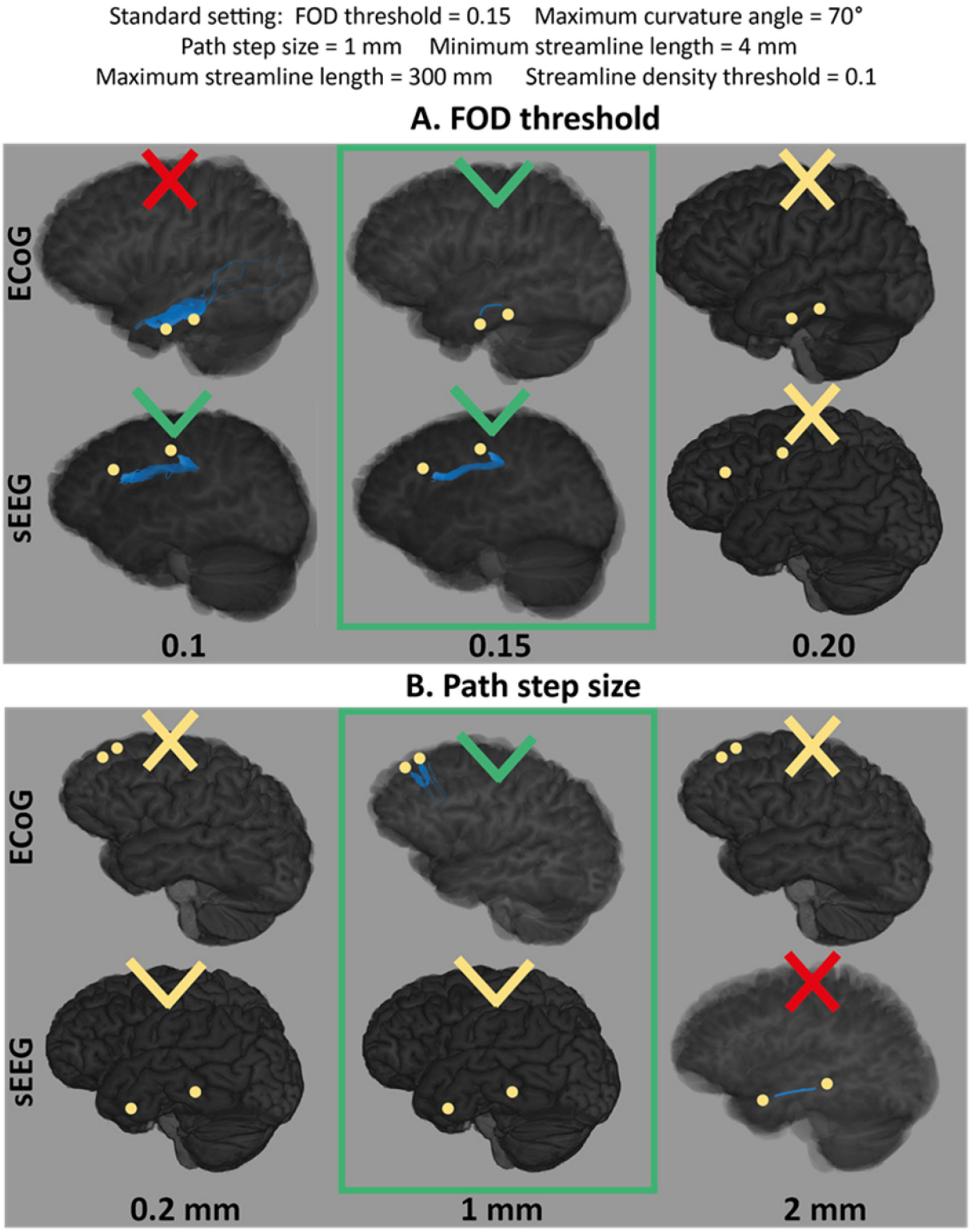

Figure 3.7: See next page.

Standard setting: FOD threshold = 0.15 Maximum curvature angle = 70°
Path step size = 1 mm Minimum streamline length = 4 mm
Maximum streamline length = 300 mm Streamline density threshold = 0.1

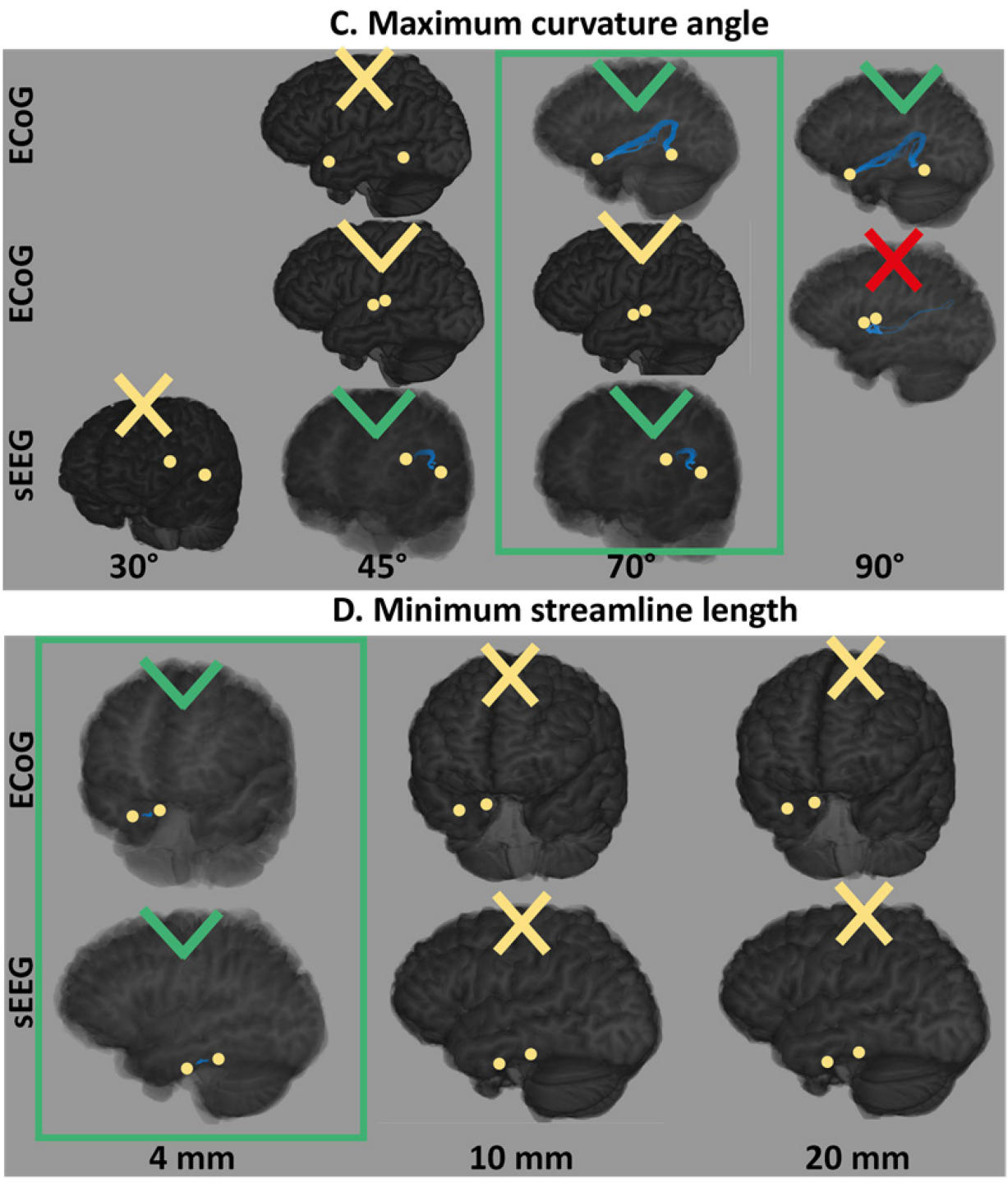

Figure 3.7: See next page.

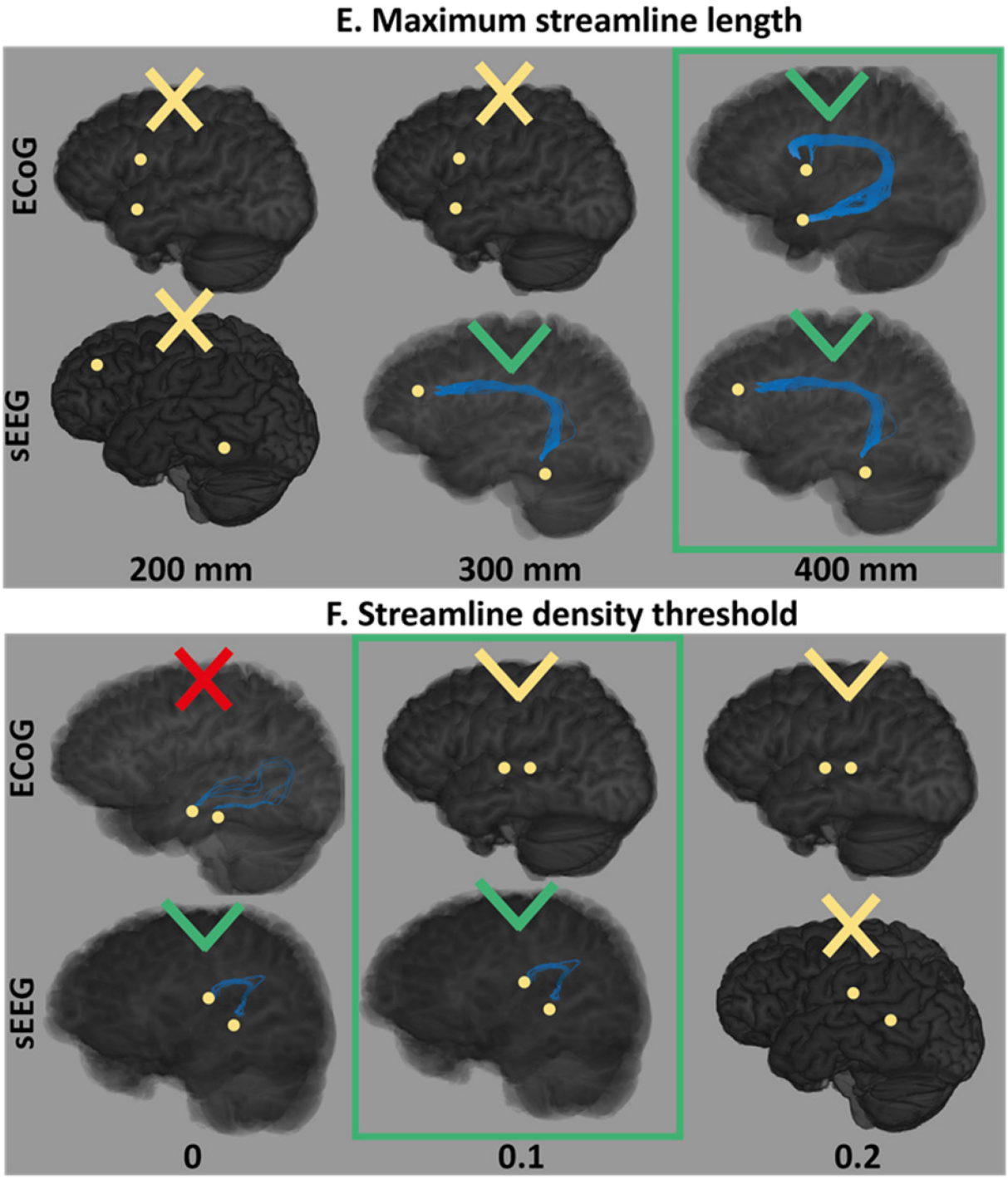

Figure 3.7: Examples of structural connections formed with varied parameter settings. The electrode contact areas (yellow) and streamlines (blue) are displayed into a 3D rendering of the de-skulled MRI-DWI. Plausible connections are indicated with a green checkmark and spurious connections with a red X. Absent connections are indicated with a yellow checkmark, when they were restricted spurious connections thus their restriction is good, and a yellow X when a plausible connections was restricted. The optimal parameter setting is encircled in green. A) With a FOD threshold of 0.1 extended spurious connections were observed. A FOD threshold of 0.2 resulted in restricted plausible connections. B) A path step size of 2 resulted in unrealistic straight streamlines in the 3D view and a path step size of 0.2 resulted in the restriction of plausible streamlines. C) With the maximum curvature angle of 70° plausible connections with highly curved, but not unrealistically curved streamlines were formed. D) A minimum streamline length of 4 mm resulted in plausible connections when closely observed in a 3D view. E) Long plausible connections with streamlines following the arcuate fasciculus required a maximum streamline length of 400 mm. F) A streamline density threshold of 0 resulted in spurious connections and a streamline density of 0.2 resulted in the restriction of plausible connections.

3.4 Discussion

We aimed to construct an iEEG constrained fiber tractography algorithm that reliably finds streamlines between electrode contacts. In a parameter optimization approach, we found the following optimal values: a FOD threshold of 0.15, a path step size of 1, a maximum curvature angle of 70°, a minimum streamline length of 4 mm, a maximum streamline length of 400 mm, and a streamline density threshold of 0.1. Especially, the FOD threshold, path step size, and streamline density threshold seemed to have a large effect on the performance of the FT algorithm. We conclude that the iEEG constrained FT algorithm can be used for the characterization of structural networks.

We observed an equivalent effect of the parameter variation in the sEEG and ECoG patients. We expected the ECoG patients to have more curved streamlines because of the subcortical U-fibers located underneath the electrode locations. Although we observed highly curved plausible connections in sEEG patients too, especially the arcuate fasciculus and the uncinated fasciculus were often tracked.

Tournier et al. visually evaluated the effect of parameter settings of the iFOD2 algorithm for whole-brain tractography [56]. They concluded that a small FOD threshold introduces more connections and a large FOD threshold results in restricted plausible connections. For the path step size, a path step size of 2 resulted in unrealistic straight streamlines and a path step size of 0.2 resulted in the restriction of plausible streamlines. This is in accordance with our results. Varying the FOD threshold, path step size, and streamline density threshold in our study resulted in a large effect on the network density. For the maximum curvature angle, maximum streamline length, and minimum streamline length changes in the parameter setting resulted in mostly extended or restricted parameters and the network density did not vary much. This indicates that these parameters did not have a large effect on the performance of the algorithm.

There are some differences between our method and the methods used by other research groups to perform iEEG constrained FT. Silverstein et al. used anatomically-constrained whole-brain probabilistic tractography instead of only seeding from priorly defined areas [38]. Whole-brain tractography is assumed more reliable than seeding from pre-defined areas in finding plausible connections because it takes the uncertainty of a connection into account by setting a desired number of streamlines. The algorithm keeps seeding randomly until this number of streamlines, fulfilling the propagation rules defined by the parameters, is tracked. The probability that the amount of streamlines between two electrode contacts exceeds the streamline density and a structural connection is formed, is thus weighted against the probability of all possible connections in the brain. The disadvantage of whole-brain tractography is the long run time, especially when using high seed densities. Whole-brain tractography is not done in this study because we wanted a sensitive algorithm, which required a too high seed density to characterize a reasonable amount of structural connections

Parker et al. seeded from priorly defined areas and reported a structural network density of 11% (range: 6-17%), which is comparable to our findings of 17% (range: 6-23%) [25]. They also used the iFOD2 algorithm with a lower FOD threshold of 0.1 and a smaller path step size of 0.2 mm. They acquired the DWI data with lower $b_1$value and more b_0 scans. Since the ideal setting of the parameters largely depends on the acquisition parameters for the DWI data, it is difficult to compare between our and Parkers iEEG constrained FT algorithm.

3.4.1 Strengths and limitations

A strength of this study is that we used both sEEG and ECoG which allowed a comparison between the configurations using the same DWI acquisition protocol and processing.

Our acquisition protocol did not meet the high angular resolution diffusion imaging (HARDI) conditions. The HARDI conditions are a theoretical requirement to assure a high enough image quality for advanced processing techniques such as constrained spherical deconvolution and higher-order integration over the FODs [24], [65]. To meet the HARDI conditions the DTI data must be acquired with high and varying b values ($up\ to\ 3000\ ^{s}/_{mm^2}$) and many diffusion directions (> 45 directions). Our DWI acquisition procedure meets the diffusion directions criterium but not the b value criterium. When scans fulfilled the HARDI criteria, the results might have had a higher sensitivity. In a clinical workflow this is not feasible due to long scan times up to a few hours [66]. Recently, more studies used advanced processing techniques without a HARDI acquisition procedure [13], [25], [38]. This is successful due to the advanced pre-processing techniques that improve image quality without the need for longer acquisition times.

A limitation of this study is that we did not validate the FT algorithm against the golden standard of post-mortem validation. In our parameter optimization, we visually inspected formed connections and compared them between different parameter settings. Visually inspection of formed connections is a cumbersome, time-consuming task thus it was not possible to inspect all connections formed with all possible parameter combinations as done in Chapter 2. We used a more pragmatic approach which was earlier used in FT studies by varying the parameters one by one and comparing them to the standard parameter setting. We only checked the 5% connections with a large difference in streamline density between the standard and varied settings. In practice, that means that we mostly checked connections that are only formed in either the standard or a varied parameter setting. By checking these connections, we were able to get an indication of the effect of the algorithm parameters on the FT algorithm performance. A disadvantage of this approach is that we do not know the performance of the FT algorithm for all connections. Besides, we did not evaluate if any combination of varied parameters performed better than the standard setting.

3.4.2 Future perspectives

There have been other methods proposed to validate the performance of FT algorithms. Our FT algorithm could be validated against a population-average atlas of white matter tracts, either extracted from DWI data or histologically derived [67]. A more methodologic strategy is the use of a synthetic phantom model combined with simulated DWI data [68]. With a synthetic phantom model white matter tracts with specific characteristics could be specified, after which the model simulates DWI data to test if the FT algorithm can characterize these tracts.

The large differences in DWI acquisition and subsequent difference in FT algorithms between studies indicate the need for a general approach for an iEEG constrained fiber tractography algorithm. We recommend evaluating the robustness of FT algorithm parameter settings by measuring the overlap between structural networks reconstructed with data from DWI scans with different acquisition parameters in the same patient.

We intended to make a sensitive algorithm but there is always a tradeoff between sensitivity and specificity. We recommend comparing the network characteristics of structural networks made with both sensitive and specific parameter settings to evaluate the effect of parameter choice on structural networks. A method to reduce false positive streamlines is the ensemble method that combines various FT algorithms with different parameter settings [69]. False negative streamlines due to noise and artifacts could be reduced by improving the acquisition procedure. With the low-resolution MRI sequence used in this study, the most pronounced distortions are present in the temporal and frontal lobes. This is also the location of most of the iEEG electrodes in this study. Therefore, it may be beneficial to look into more advanced acquisition methods that improve the signal-to-noise ratio without substantially increasing the scan times. For epilepsy patients, acquiring the DWI data with high field strengths of 7T could be a feasible option since 7T MRI is already clinically used in some of these patients [70].

We noticed that a part of the biologically implausible streamlines had an unrealistic long length. We recommend to determine the maximal streamline length individually per pair of electrode contact areas based on the expected length of the white matter track. With a population-average atlas of the white matter tracts characterized by FT this expected length of streamlines between two brain areas could be extracted [67].

3.4.3 Conclusion

We developed an iEEG constrained FT algorithm based on the iFOD2 algorithm to characterize structural networks. The optimized FT algorithm parameters are a FOD threshold of 0.15, a maximum curvature angle of 70°, a minimum streamline length of 4 mm, a maximum streamline length of 400 mm, a path step size of 1 and a density threshold of 0.1. The algorithm was able to characterize plausible connections between electrode contact areas. In the next chapter, we compared structural networks characterized with this algorithm to effective networks.

4. The analogy between structural brain networks obtained from diffusion weighted imaging and effective networks derived from single pulse electrical stimulation

4.1 Introduction

Since the first epilepsy surgery in 1886, people with increasingly complex epilepsies could be successfully treated due to constant improvement of surgical strategies and pre-operative investigations. Initially, epilepsy surgery focused on the removal of visible lesions. Then, epilepsy surgery focused on the removal of a more conceptual epileptogenic zone (EZ). The EZ is the cortical area that must be removed to achieve seizure freedom. With the current approach to delineate this EZ, 25-50% of the surgical candidates do not become seizure-free [6]. A network approach that focusses on diseased connections in a brain's network, rather than just the EZ, might improve the surgical outcome [29].

There are different approaches to characterize brain networks: functional, effective, or structural networks. In this study, we focus on effective and structural networks. Effective networks describe the causal influence between brain areas by perturbating one area with for example single pulse electrical stimulation (SPES) [27]. With SPES, a local population of neurons is activated by applying electrical stimuli to adjacent intracranial electrode contacts. The responses in all other electrode contacts are analyzed to reveal the effective connections between underlying brain areas. Structural networks describe the anatomical connections between brain areas via white matter tracts and can be determined with diffusion weighted imaging (DWI). DWI is a magnetic resonance imaging (MRI) technique that captures the anisotropic diffusion of water molecules along myelinated axons to estimate the spatial organization of the white matter [13]. With fiber tractography (FT), the specific paths of white matter tracts between areas of interest, such as electrode contacts, could be reconstructed, allowing identification of structural networks [14].

Comparing structural and effective networks benefits understanding of how epilepsy alters the complex brain network [29]. The structural connections can non-invasively reveal the biologically plausible pathways that give rise to the observed effective connections between brain areas covered by intracranial electrodes. Two studies compared structural and effective brain networks [25], [51]. Crocker et al. measured a high Pearson correlation of 0.68 ± 0.21 between physiological effective and structural networks [51]. Parker et al. found a low correlation (0.13 ± 0.066) and suggested that the two networks can complement each other in explaining how epilepsy influences the patient's brain network organization[25]. Effective networks had greater outward connectivity at the ictal-onset zone, while structural networks showed greater connectivity within the ictal-onset zone. Parker et al. did not analyze to what extent these findings could be described by epilepsy related pathophysiological processes and what the influence of sources of error like modality specific artifacts and bias due to irregular spatial sampling was. Crocker et al. corrected for the bias of irregular spatial sampling and reported a significant influence of this bias on the correlation [51]. They only considered physiological networks and did not study specific network characteristics. The large difference in reported correlation between the two studies indicates the need to further elucidate the relation between structural and effective networks using specific network characteristics and by taking the influence of epilepsy and bias into account.

We aimed to elucidate how structural and effective networks interrelate and how epilepsy alters this relation. We assessed the intermodal similarity between structural and effective networks of focal epilepsy patients. We applied graph analysis to further specify correlating network characteristics. We constructed a linear multilevel model to analyze the influence of epilepsy and sources of bias on the correlation between structural and effective networks. This research is a preliminary step in comparing

structural and effective networks to assess the influence of epilepsy on brain networks for a network based surgical strategy.

4.2 Methods

4.2.1 Patient specification

We selected data from people with drug resistant focal epilepsy who underwent both a diffusion weighted MRI and long-term, invasive EEG (iEEG) monitoring between 2018 and 2021. Inclusion criteria were the presence of a DW image, a 3DT1-weighted MRI, a post-implementation CT scan, and a SPES procedure. The clinical data were extracted from the RESPect database that consists of iEEG data from epilepsy surgery candidates treated at the University Medical Center Utrecht, the Netherlands [57]. Written informed consent was obtained and the Medical Ethical Committee of the UMC Utrecht approved the use of coded data in the RESPect database for retrospective research.

DWI acquisition
DWI was acquired with a multi slice, multi shot echo-planar imaging (EPI) sequence with a TE of 91 ms, TR of 3191 ms, and a resolution of 2 x 2 x 2 mm^3. A total of 62 diffusion sensitizing gradient directions with a b value of 1600 $^{s}/_{mm^2}$ and a single b_0 scan were obtained**.** The 3D T1 MRI and CT were acquired with a resolution of 1 x 1 x 1 mm^3. A 3D T1 was acquired at the time of the DWI scan for anatomical reference ('MRI-DWI'). For processing of the electrode locations we used another 3D T1 acquired before electrode implantation ('MRI-CT').

iEEG recording and SPES
iEEG data were recorded at 2048 Hz with a MicroMed LTM64/128 express EEG headbox with an integrated programmable stimulator (MicroMed, Mogliano—Veneto, Italy). The placement and type of the intracranial electrodes were determined clinically. Subdural electrode grids (ECoG) had an interelectrode contact distance of 1 cm and consisted of platinum electrode contacts with a 4.2 mm^2 contact surface embedded in silicone (Ad-Tech, Racine, WI). Cylindrical depth electrodes (sEEG) were either platinum contacts with an 8.3 mm^2 contact surface and 5 mm interelectrode contact distance (Ad-Tech, Racine, WI) or platinum/iridium contacts with a 5.0 mm^2 contact surface and 3.5 mm interelectrode distance (DIXI Medical, France). We excluded electrodes not placed in the grey matter or recording noisy signals from further analysis. SPES consisted of one trial for each pair of adjacent electrode contacts. Each trial consisted of ten monophasic pulses with a pulse width of 1 ms, a current of 1-8 mA, and a repetition rate of 0.2 Hz.

4.2.2 Structural networks

The DWI was processed using the MRtrix3 package and MATLAB version R2021b (The Mathworks Inc., Natick, Massachusetts), combined with the brain imaging toolboxes Freesurfer, FSL, ANTs, and SPM12 [58]. The DWI data were denoised and corrected for common distortions following the pipeline proposed by Ades-Aron et al. [71]. In short: consecutively Marchenko-Pastur Principal Component Analysis (MP-PCA) denoising, Gibbs ringing correction, EPI distortion correction, Eddy current correction, movement distortion correction, b0 field inhomogeneity correction, and b1 bias field correction was performed. The MRI-DWI was linear co-registered to the DWI b_0 image using the SPM12 toolbox.

The post-implantation CT scan was linear co-registered to the MRI-CT as the reference image and intracranial electrode contact coordinates were extracted from the CT scan (see Figure 4.1). We transformed the electrode contact coordinates to the DWI space via co-registration of the MRI-CT to the MRI-DWI. The inverse transformation matrix was used to transform the electrode contact coordinates. The MRI-DWI was used as the anatomical constraining image for fiber tractography. We segmented the MRI-DWI in six binary brain masks containing cortical grey matter, subcortical grey

matter, white matter, the grey-white matter boundary, cerebrospinal fluid (CSF), and if present, pathological tissue. The electrode contact coordinates were projected onto the grey-white matter boundary mask to create electrode contact areas. These electrode contact areas were used as seed and termination regions for fiber tractography. The nearest 64 voxels in the grey-white matter boundary were assigned to each electrode contact area. The volume of the electrode area of 64 mm^3 was chosen such that it was comparable to the estimated size of the locally activated brain area with SPES. Overlapping voxels were assigned to the nearest electrode contact, which resulted in some contact areas having a volume of less than 64 mm^3.

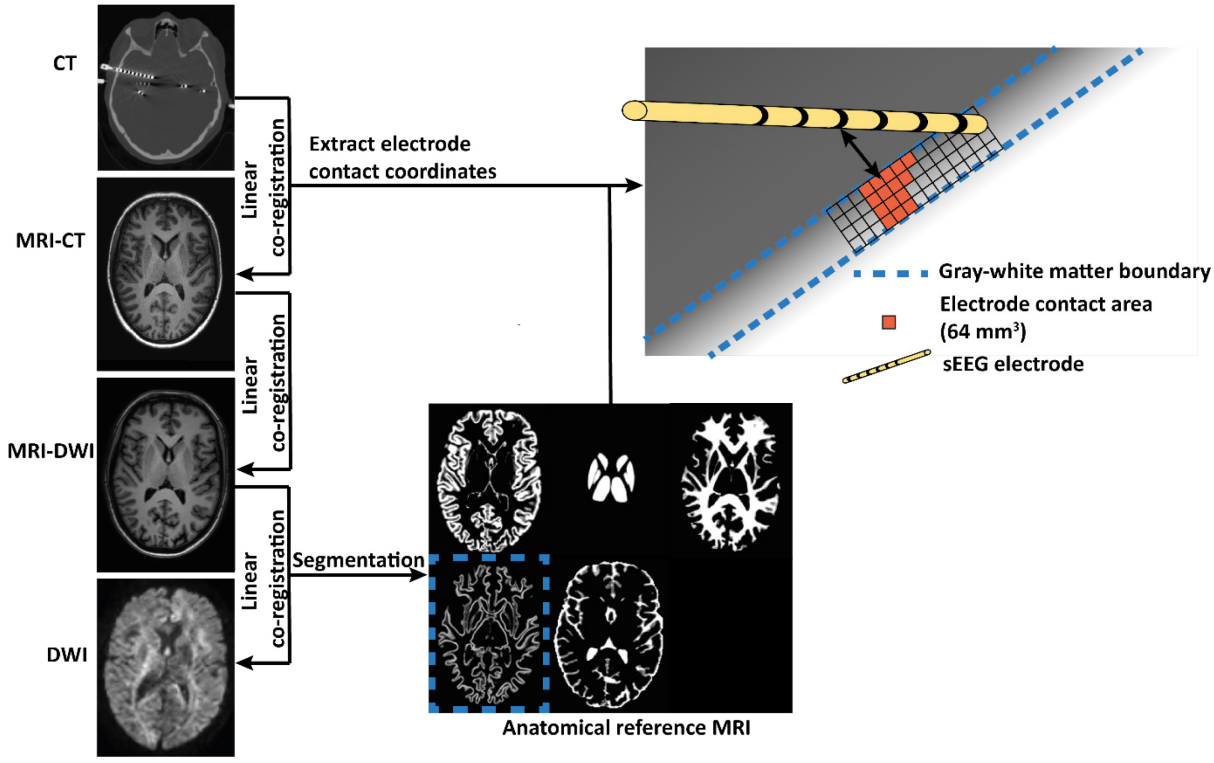

Figure 4.1: Schematic overview of the co-registration and electrode contact area definition.

Structural networks were reconstructed by fiber tracking the white matter tracts between iEEG electrode contact locations. Anatomical constrained probabilistic tractography was performed using the iFOD2 reconstruction algorithm with a seed density of 6000 seeds per voxel and constraints on the diffusion strength (FOD (fiber orientation distribution)-threshold), maximal angle, minimal streamline length, and maximal streamline length. The FOD threshold was 0.15, the maximal angle was 70, and the minimal and maximal streamline length was respectively 4 mm and 400 mm. The response function for constrained spherical deconvolution (CSD) was estimated from the DWI data with the dHollander algorithm [72]. The fiber orientation distribution was calculated with the Multi-Shell Multi-Tissue CSD (MSMT-CSD) algorithm using two-tissue CSD [56].

We created binary structural networks with every node representing an electrode area. The streamlines seeded inside an electrode area and terminated inside another electrode area were considered. The streamline density was calculated by the number of streamlines divided by the volume of the two involved electrode contact areas. A structural connection was formed when the streamline density exceeded a threshold of 0.1.

4.2.3 Effective networks

The 10 stimuli of each SPES trial were epoched in a time window 2s prior and 2s post stimulus, time-locked to the stimulus artifact. These ten epochs for each trial were averaged per electrode contact and the baseline 2 s pre-stimulation was subtracted. The obtained post-stimulus signal is called the evoked response potential (ERP). Early responses (ERs) were detected in this ERP using an automatic

detector. For ECoG data, ERPs were classified as ER if they occurred within 9-100 ms after the stimulation and the amplitude exceeded 2.6 times the standard deviation of the baseline before stimulation. For sEEG data, the ERP had to exceed 3.5 times the SD of the baseline. We created binary effective networks with every node representing an electrode area. Connections were drawn from both electrode contacts in a stimulus pair to the electrode contacts in which an ER was detected. Effective networks were made symmetrical by considering all ERs as bi-directional, to be able to compare to the non-directional structural networks.

4.2.4 Inter-modal similarity

The inter-modal similarity between structural and effective networks was determined with the Jaccard Index (JI) calculated as the size of the set of intersecting connections divided by the size of the set of union connections:

$$\text{Jaccard Index } (JI) = \frac{SC \cap EC}{SC \cup EC} \tag{5.1}$$

with SC and EC the structural and effective connectivity matrixes. The Jaccard similarity test was conducted to statistically determine if the JI was higher than expected by chance given the densities of the networks [73]. The expected JI is the JI when the connections are placed at random positions in the network, calculated with:

$$JI_{\text{expected}} = \frac{d_{SC} d_{EC}}{d_{SC} + d_{EC} - d_{SC} d_{EC}} \tag{5.2}$$

with d_{SC} and d_{EC} the densities (see Equation 3.1) of the structural and effective connectivity matrixes SC and EC.

4.2.5 Network topography

We performed graph analysis to compare the topography between structural and effective networks. We analyzed the network characteristics degree and betweenness centrality. Each network characteristic was calculated per electrode contact area. To evaluate the impact of the irregular spatial sampling of the brain with sEEG or ECoG, we determined the correlation between the node proximity and the degree. The node proximity per node was defined as the median distance between this node and all other nodes. The distance between two nodes is computed as the mean Euclidean distance between electrode contact coordinates extracted from the post-implementation CT scan. We used Spearman's ρ test to calculate the correlation between the node proximity and the degree per patient for both the structural and effective networks.

The correlation between structural and effective networks for the degree and betweenness centrality per patient was determined with the spearman's ρ test. The network characteristics that showed a correlation between structural and effective networks at patient level were further assessed at group level with linear multilevel analyses. We used the network characteristic of the structural network as dependent variable. We first fitted an intercept-only model to quantify the dependency in the data with the intra class correlation (ICC). The ICC was calculated as:

$$ICC = \frac{\sigma^2_{between}}{\sigma^2_{within} + \sigma^2_{between}} \tag{5.3}$$

with $\sigma^2_{between}$ and σ^2_{within} the variance of the data between patients and within patients respectively. We constructed a linear multilevel model with backward elimination of possible predictors. The possible predictors at patient level were the effective network characteristic, the node proximity, the volume of the structural electrode contact areas, and the nodes in the seizure onset zone (SOZ). The treating neurophysiologist of each patient determined which electrode contacts were located on the

SOZ independently of this study. We added each variable as fixed effect to the model. The variable with the highest p-value was removed at each step until all variables had a p-value<0.05. For the variables in the final model, we concluded that they are associated with the structural network characteristic.

Statistical analyses were performed in R 4.1.2 [74]. We corrected for multiple comparisons with the Benjamini-Hochberg procedure. The individual critical p-values for statistical significance were calculated as:

$$p_{max} = \frac{i}{m} * 0.05 \quad (5.4)$$

with i the individual p-value's rank and m the number of patients.

4.3 Results

4.3.1 Patient specification

We selected thirteen patients with a median age of 25 (range= 10-50). Eight patients underwent sEEG and five patients underwent ECoG (see Table 4.1).

Table 4.1: Patient specification of the patients with ECoG (first 5 patients) and sEEG (last 8 patients). m = male; f = female; F = frontal; T = temporal; P = parietal; C = pre or post-central gyrus; O = occipital; IH = interhemispheric; A = amygdala; H = hippocampus; I= insula R=right; L=left; ND = not determined; mMCD = mild malformation of cortical development; FCD = focal cortical dysplasia; NP = no pathology found; NR = not resected. In two patients the SOZ could not be determined due to diffuse seizure onset. In one patient the SOZ is not resected due to overlap of the SOZ with functional area. The outcome is determined by the ILAE classification.

Patient	ECoG/ sEEG	Age at iEEG	iEEG location	Sampled hemisphere	Included electrodes (all electrodes)	Electrodes in SOZ	Outcome (months follow up)	Pathology
1	ECoG	15	T,P,O	L	104 (112)	37	5 (13)	NP
2	ECoG	28	T	L	71 (72)	4	5 (25)	mMCD
3	ECoG	37	F	L	61 (64)	4	NR	NR
4	ECoG	44	F,T,IH	L	71 (80)	15	1 (7)	FCD type 2A
5	ECoG	18	F,T	L	58 (64)	11	3 (17)	mMCD
6	sEEG	45	F,T,A,H	R	44 (67)	14	1 (30)	DNET grade 1
7	sEEG	50	F,T,A,H	R & L	47 (88)	4	1 (27)	NP
8	sEEG	50	T,P,A,H	R	52 (78)	9	2 (7)	Gliosis
9	sEEG	25	F,T	R & L	101 (121)	ND	NR	NR
10	sEEG	17	T,P,O,A,H	R	68 (90)	21	2 (10)	mMCD
11	sEEG	17	F,C,T,P,I	L	47 (89)	11	1 (7)	mMCD
12	sEEG	14	F,T,A,H,I	L	58 (103)	4	5 (13)	mMCD
13	sEEG	10	F,T,A,H,I	L	81 (142)	ND	NR	NR

4.3.2 Inter-modal similarity

The inter-modal similarity, measured with the JI, between structural and effective networks, was 0.25 (interquartile range (IQR)= 0.19-0.29). The JI was for all patients significantly higher ($p< 0.0001$) than expected by chance given the densities of the networks (see Table 4.2). In Figure 4.2, the union and

intersecting connections in the networks were visualized for a patient with a high JI and a low JI. The intersecting connections of a patient with a low JI were primarily between neighboring electrode areas.

Table 4.2: The inter-modal similarity determined by the JI was for all patients significantly higher than the expected JI.

Patient	Expected JI	Observed JI	P-value
1	0.14	0.19	<0.0001
2	0.14	0.26	<0.0001
3	0.23	0.38	<0.0001
4	0.10	0.18	<0.0001
5	0.19	0.36	<0.0001
6	0.08	0.27	<0.0001
7	0.05	0.17	<0.0001
8	0.15	0.28	<0.0001
9	0.05	0.22	<0.0001
10	0.08	0.19	<0.0001
11	0.20	0.30	<0.0001
12	0.06	0.23	<0.0001
13	0.07	0.25	<0.0001

Figure 4.2: Connectivity matrixes of two patients. Left: structural connectivity matrix in blue. Middle: effective connectivity matrix in green. Right: Union (blue & green) and Intersection (orange) of structural and effective connectivity matrixes. A: ECoG patient 5 with high JI. Structural and effective connections are present in the same areas. B: ECoG patient 4 with low JI. We see mainly effective connections between neighboring electrode areas.

4.3.3 Network topography

The node proximity showed a significant negative correlation with the degree of structural networks in 10/13 patients and a significant positive correlation in one ECoG patient (see Figure 4.3). In 12/13 patients, a significant negative correlation existed between the node proximity and the degree of effective networks (see Figure 4.4). The nodes in de SOZ had often low node proximity.

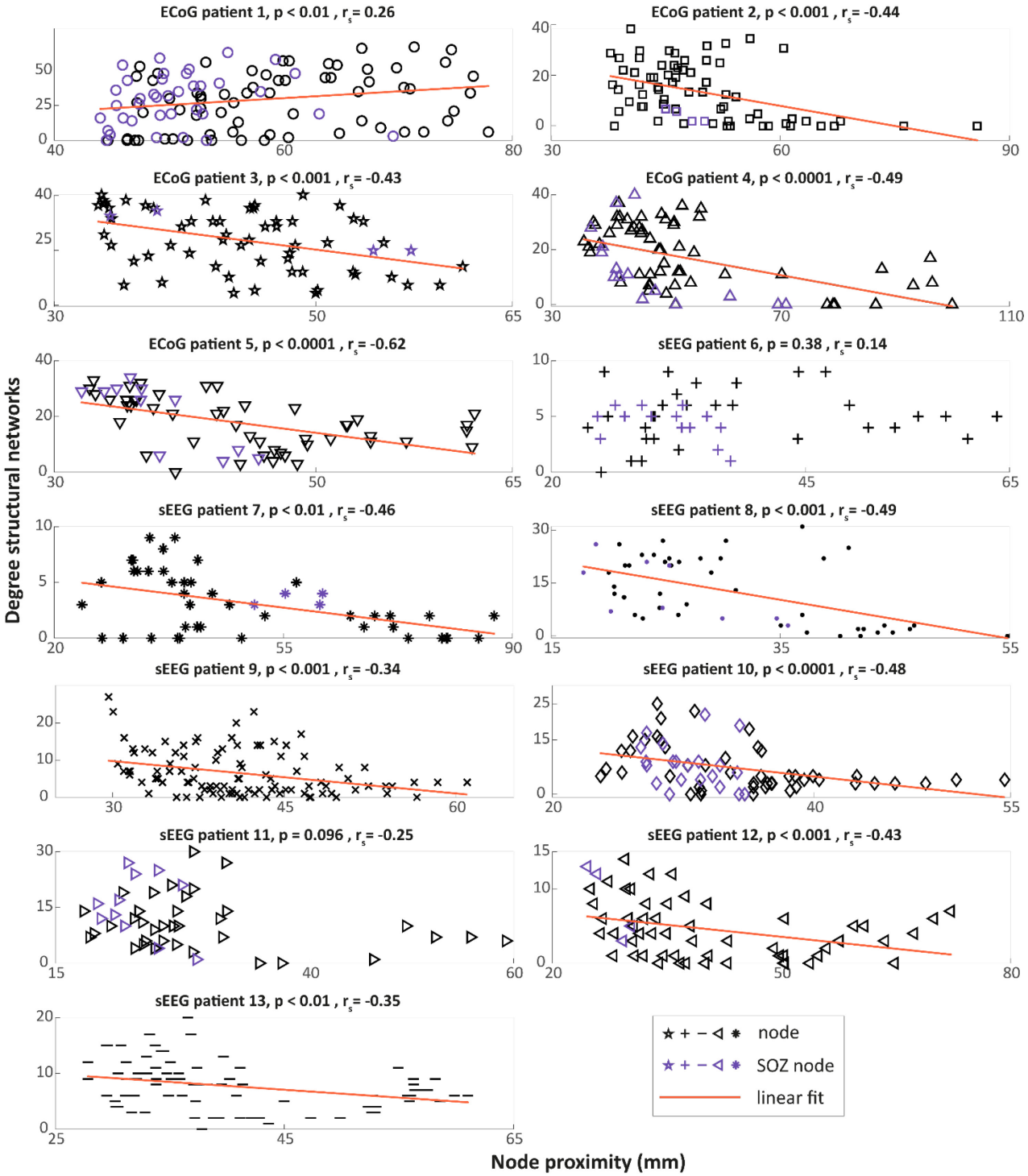

Figure 4.3: Correlation between the node proximity and the degree of structural networks. In 10/13 patients the node proximity was negatively correlated with the degree of structural networks. We computed a positive correlation in ECoG patient 1 and no significant correlation in sEEG patients 6 and 11. The orange lines are the best linear fit through the data points. The purple markers indicate the seizure onset zone (SOZ). In patient 9 and 13 the SOZ was not determined. In patients 2, 6, 7, 10, 11 and 12 the SOZ nodes cluster with regards to the node proximity.

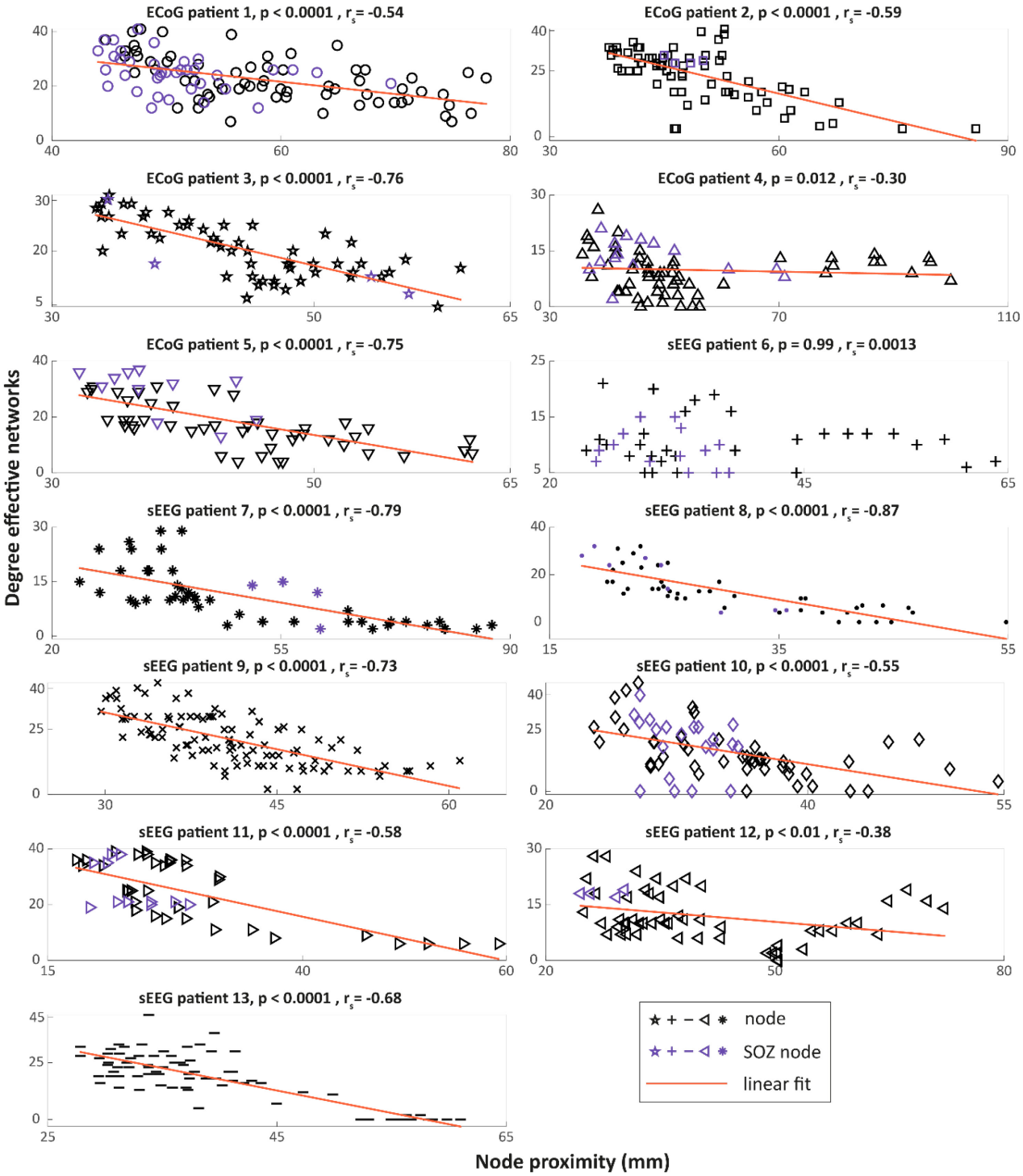

Figure 4.4: Correlation between the node proximity and the degree of effective networks. In 12/13 patients the node proximity was negatively correlated with the degree of effective networks. We computed no significant correlation in sEEG patient 6. The orange lines are the best linear fit through the data points. The purple markers indicate the seizure onset zone (SOZ). In patient 9 and 13 the SOZ was not determined. In patients 2, 6, 7, 10, 11 and 12 the SOZ nodes cluster with regards to the node proximity.

We observed a positive correlation between the degree of effective networks and the degree of structural networks in 9/13 (see Figure 4.5). The nodes in de SOZ did not cluster. For the betweenness centrality, we did not find a significant correlation in the sEEG patients and no consistent significant positive (2 patients) or negative (1 patient) correlation in the ECoG patients thus we did not further assess this correlation at group level (see Table 4.3).

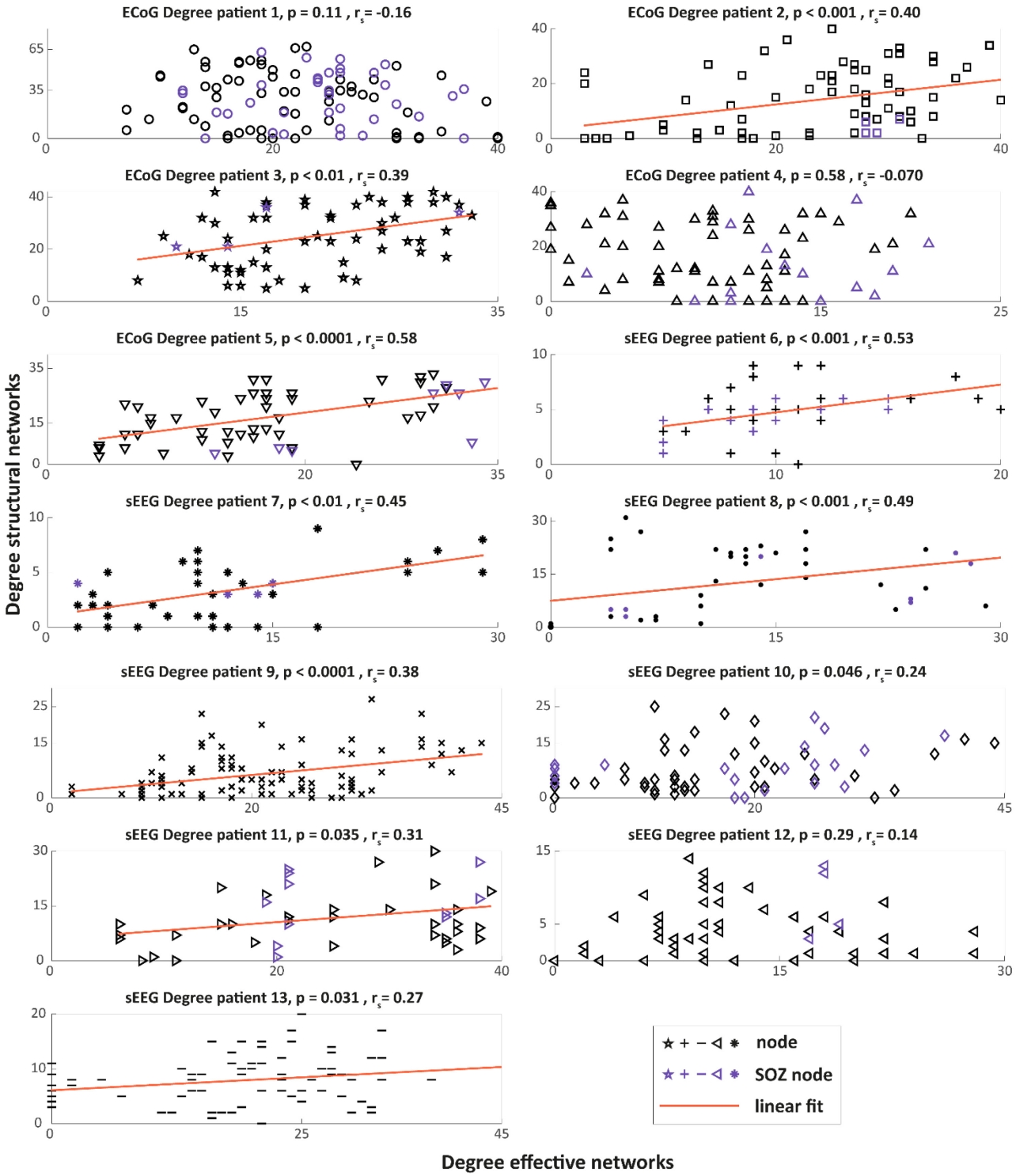

Figure 4.5: Correlation between the degree of effective and structural networks. A positive correlation existed between the degree of structural and effective networks in 9/13 patients. Four patients, ECoG patients 1 and 4, and sEEG patients 10 and 12 showed no significant correlation. The orange lines are the best linear fit through the data points. The purple markers indicate the seizure onset zone (SOZ). In patient 9 and 13 the SOZ was not determined.

Table 4.3: Correlation between the betweenness centrality of structural and effective networks per patient. In 2/5 ECoG patients, the betweenness centrality of the structural networks was positively correlated to the betweenness centrality of the effective networks. In 1/5 ECoG patients, we computed a negative correlation. In the rest of the patients no significant correlation was found.

	Patient	1	2	3	4	5	6	7	8	9	10	11	12	13
Betweennes Centrality	**P-value**	0.011	<0.001	0.047	0.67	<0.01	0.18	0.06	0.23	0.59	0.38	0.15	0.07	0.69
	R_s	-0.25	0.39	0.26	-0.05	0.39	0.2	0.27	0.17	0.05	0.11	0.21	0.24	-0.05

The linear multilevel model showed that the node proximity and the degree of the effective networks are significantly associated with the degree of the structural network (see Table 4.5). For the models which included the SOZ nodes, we included the eleven patients with a defined SOZ. The ICC was 0.37, which indicates that a considerable amount of the variance in the data was caused by the between patient variance. The degree of effective networks was positively correlated to the degree of structural networks after accommodating for node proximity with a regression coefficient (β) of 0.11 (p-value = 0.016). The node proximity was negatively correlated to the degree of structural networks at a group level with a regression coefficient (β) of -0.15 (p-value < 0.0001), in concordance with Figure 4.3.

Table 4.5: The characteristics of the fitted linear multilevel models. The degree of the effective networks and the node proximity were significantly associated with the degree of the structural networks. β = regression coefficient. SOZ = seizure onset zone. All steps of the backward elimination are shown.

	Model with all possible predictors (n=11)	**Model without volume (n=11)**	**Final model (n=11)**	**Final model with all patients (n=13)**
Intercept	β_0 = 15	β_0 = 17	β_0 = 18	β_0 = 17
	P-value < 0.001	P-value < 0.0001	P-value < 0.0001	P-value < 0.0001
Degree effective networks	β = 0.13 (0.018 – 0.24)	β = 0.11 (0.018 – 0.24)	β = 0.12 (0.014 – 0.24)	β = 0.11 (0.021 – 0.20)
	P-value = 0.024	P-value = 0.024	P-value = 0.029	P-value = 0.016
Node proximity	β = -0.16 (-0.25 – -0.074)	β = -0.16 (-0.23 – -0.08)	β = -0.16 (-0.24 – -0.068)	β = -0.15 (-0.23 – - 0.076)
	P-value < 0.001	P-value < 0.001	P-value < 0.001	P-value < 0.0001
SOZ nodes	β = -1.1 (-3.33 – 1.07)	β = -1.1 (-3.33 – 1.07)	NA	NA
	P-value = 0.31	P-value = 0.32		
Volume electrode areas	β = 0.035 (-0.095 – 0.11)	NA	NA	NA
	P-value = 0.93			

4.4 Discussion

We aimed to assess the relation between structural and effective networks and explore how epilepsy alters this relation. We found a moderate inter-modal similarity between structural and effective networks with a JI of 0.25 (IQR: 0.19-0.29). The degree of the structural networks compared to the effective networks at patient level showed a positive correlation in 10/13 patients. We did not find a consistent significant positive or negative correlation at patient level for the betweenness centrality of the structural networks compared to effective networks. After controlling for the bias caused by the node proximity and the between patient variance with multilevel modeling, the correlation between

the degree of structural and effective networks is still present at group level. We did not find statistical evidence that epilepsy alters the relation between structural and effective networks.

Our findings regarding the inter-modal similarity are in concordance with Parker et al. They reported a JI of 0.18 ± 0.024 for the binary networks and a Pearson correlation of 0.13 ± 0.066 for weighted networks [25]. Crocker et al. reported a correlation for weighted networks of 0.68 ± 0.21 [51]. The Pearson correlation only takes the union connections into account. When the inter-modal similarity is low, the correlation describes a small part of the network and we must be careful interpreting this finding. Crocker et al. corrected for the node proximity using the distance between electrode contacts and reported a negative correlation between the node proximity and the connectivity strength of both the structural and effective networks. This is in accordance with the negative correlation between node proximity and degree we reported.

No previous studies explicitly compared the topography between structural and effective networks. Parker et al. reported altered structural and effective connectivity around the ictal-onset zone but did not correct for node proximity [25]. Since the presumed SOZ is extensively sampled in sEEG and often located in the middle of the ECoG, this correction is necessary to be able to make valid conclusions. Van Blooijs et al. corrected for node proximity and reported a significantly higher degree in the SOZ in effective networks [27]. The SOZ was not a significant predictor in the multilevel model that described the correlation between the degree of structural and effective networks. This may suggest that network alterations due to epilepsy are similar in structural and effective networks. However, only four patients were seizure-free in our study which made the SOZ as measure of epilepsy less reliable and may have introduced noise into the multilevel model. Therefore we must be careful to conclude that epilepsy did not alter the relation between structural and effective networks.

We observed an equivalent correlation between structural and effective networks in the sEEG and ECoG patients. For three patients, ECoG patient 1, 4, and sEEG patient 12 (see Figure 4.5) we did not find a significant correlation for the degree between structural and effective networks . This could be due to modality dependent sources of error in the structural or effective networks. For structural networks, noise or artifacts in the DWI data could have led to incorrect FOD reconstruction which may have blocked the path of the streamlines between two electrode contacts. In patient 4, the focal cortical dysplasia possibly altered the grey-white matter boundary which may have disturbed the seeding of streamlines in that area. For effective networks, volume conduction between nearby electrode contacts could have led to more short distance connections compared to structural networks.

The exact relation between structural and effective networks remains a complex question. Theoretically, effective connections describe the physiological organization of communication between brain areas. Structural networks could be seen as the supporting hardware that allows this communication. This assumption does not fully explain the relation between structural and effective networks. The structural connections could be non-functional, or communication could go via other ways than the white matter pathways the structural connections are inferred from, for instance via hormonal or cell-to-cell communication [75],[76]. Some studies hypothesize that especially in epileptogenic network parts, the structure-function coupling is disrupted [25],[77]. This may be an explanation of the moderate correlations we reported and indicate that structural and effective networks may be interchangeably used but also have the potential to complement each other.

4.4.1 Strengths and limitations

A strength of this study is that we used multilevel modeling to elucidate the relation between structural and effective networks which allowed us to correct for node proximity. The ICC was 0.37 which indicates that a multilevel model is necessary to analyze the correlation between the degree of structural and effective networks at group level. A limitation is that we used a small heterogeneous

dataset. Therefore we could not draw explicit conclusions on group level, but we assessed the data on electrode contact level, and focused on the comparison between nodes within one patient.

A possible cause of underestimation of the relation between structural and effective networks is the arbitrary choice of sampled brain areas for the characterization of structural networks. To determine the size of the electrode contact areas, we made an assumption about the size of the local activated brain area with SPES. This assumption and the projection onto the grey-white matter boundary probably resulted in a spatial different sampled structural network compared to the effective network. Furthermore, the volume of the electrode contact areas differed due to overlapping areas. This resulted in some electrode contact areas having a critically low volume. We used the volume as a possible predictor in the multilevel model and did not find a significant correlation with the degree of the structural networks.

4.4.2 Future perspectives

In our comparison between structural and effective networks we used binary networks. We recommend to further elucidate the relation with networks weighted by the connectivity strength. For effective networks, the amplitude and latency of the ER can be used to determine the connectivity strength. For structural networks, the streamline density and the mean FOD volume fraction describe the connectivity strength. Comparing networks weighted by the connectivity strength could result in a higher correlation because it avoids the need for subjective thresholding.

To further explain to what extent structural and effective networks interrelate, we need a method to correct for the node proximity on a patient and electrode level. The comparison of whole-brain structural networks and structural networks constrained by iEEG could be a first step. In this study, the node proximity is determined using the Euclidean distance between electrode contact coordinates. We recommend to use the average streamline length to precisely describe the node proximity of the electrode contacts in structural networks.

We were not able to conclude if epilepsy alters the relation between structural and effective network by using the SOZ as predictor in the multilevel model. A strategy to evaluate the effect of epilepsy on the relation is to compare epileptogenic and physiological networks. Defining physiological networks is challenging in the context of epilepsy as a network disorder[78], [79]. We recommend to use population-averaged networks as physiological network and compare them with patient-specific epileptogenic networks on electrode contact level. For structural networks, these population-averaged networks already exist [67]. For effective networks, we recommend to use a homogeneous patient population with approximately the same anatomical electrode configuration. Data of high density grids placed on a physiologically functioning brain area currently acquired in the UMC Utrecht could assist in the characterization of a population-averaged physiological network [80].

4.4.3 Conclusion

We explored the relation between structural and effective patient-specific brain networks as a preliminary step to establish a network based surgical strategy. We conclude that structural and effective networks show a moderate overall relation and their topography described by the degree correlates independently of common sources of bias. . We found no effect of epilepsy on the relation between these networks. We recommend to further investigate the extent of this relation and disruptions caused by epilepsy with higher sample sizes and by using population-averaged networks.

5. General discussion & conclusion

This master thesis focused on the relation between structural and effective brain networks in focal epilepsy. Our research question was: How do structural networks derived from diffusion weighted imaging (DWI) relate to effective networks obtained from single pulse electrical stimulation (SPES) in patients with focal drug resistant epilepsy?

In Chapter 2, we optimized the automatic early response (ER) detector by Van Blooijs et al. for stereo electroencephalography (sEEG) data [39]. The sensitivity, specificity, positive predictive value (PPV), and negative predictive value (NPV) of this detector were respectively 0.81,0.93,0.68, and 0.69. With this performance and a visual check of the detected evoked response potentials (ERP), the detector can be used for the characterization of effective networks.

In Chapter 3, we constructed an intracranial EEG (iEEG) constrained fiber tractography (FT) algorithm. The algorithm was able to characterize plausible connections between electrode contact areas by using state-of-the-art processing techniques. We concluded that the iEEG constrained FT algorithm can be used for the characterization of structural networks.

In Chapter 4, we tried to answer two sub-questions. The two sub-questions were '*What is the inter-modal similarity between structural networks derived from DWI and effective networks obtained from SPES*?*'* and '*What is the influence of epilepsy on the correlation between network characteristics of structural and effective networks?'* We observed a moderate inter-modal similarity determined by the Jaccard Index with a median of 0.25 (IQR: 0.19-0.29). We found a positive correlation in 10/13 patients for the degree and no consistent correlation for the betweenness centrality. The positive correlation between the degree of structural and effective networks is still present at group level, thereby accommodating for node proximity bias and between patient variance with multilevel modeling. This suggests that structural and effective networks of focal drug resistant epilepsy patients correlate but also have the potential to complement each other. To answer the second question, we included the possible influence of epilepsy in our multilevel model by specifying seizure onset zone nodes but could not draw convincing conclusions at group level due to the small amount of seizure-free patients (n=4).

Our research clarified and refined the sparse previous findings about the structural and effective brain network organization in focal epilepsy. Our reported correlation in the topography refined the finding of an overall correlation by Parker et al. and Crocker et al. We clarified the influence of node proximity observed by Crocker et al. by correcting for it on group level. In contrast to the relation between structural and effective networks, extensive efforts are made to compare structural and functional networks [29], [77]. Functional networks are another category of brain networks based on EEG, iEEG, functional magnetic resonance imaging, and magnetoencephalography [81]–[83]. Van Diessen et al. performed a review study and concluded that there is a positive correlation between structural and functional networks with similar disruptions in network topology in epilepsy patients [77]. Slinger et al. recently reevaluated these conclusions in a systematic review and could not reproduce the conclusions regarding the network topology. To what extent functional networks are constrained by structural networks remains a complex question. Preti et al. elucidated one of the complexities by using an index that quantifies the structural-functional decoupling [84]. They discovered that the structure-function coupling is spatially varying over brain regions with lower and higher level functions.

5.1 Strengths and limitations

This is the first study that explicitly compared the topography between structural and effective networks by using network characteristics and taking the influence of node proximity into account. We used both sEEG and ECoG which allowed a comparison between the configurations. We only analyzed patient-specific data and focused on comparisons within patients. Since the surgical trajectory is highly patient-specific this is a strong methodology that allows future clinical translation. A limitation is that

we were not able to perform sub analysis, for instance, to analyze the influence of epilepsy in seizure-free patients, due to our small sample size.

We gained insights into the practical and methodological strengths of structural and effective networks. Effective networks are the most direct measure of connectivity due to direct perturbation and recording of neural activity which allows a high precision but low spatial coverage. Structural networks can identify anatomical connections that can be located and disconnected in a surgical setting thus allowing potentially an easy clinical translation. Caution is needed in the structural network characterization of focal epilepsy patients with large white matter abnormalities or structural lesions affecting the grey-white matter boundary. Our FT algorithm used to characterize structural networks might perform differently in those areas but is potentially useful in describing the deviated structural pathways around those lesions. Validation of our FT algorithm using a population-averaged atlas is needed.

5.2 Future perspectives

Current insight into the relation between structural and effective networks in focal epilepsy patients is yet insufficient to elucidate how structural networks, effective networks, or a combination could be used to establish a network based surgical strategy.

The experience in epilepsy surgery is that often an integration of techniques is needed to define the epileptogenic zone with enough certainty to achieve seizure freedom. This experience illustrates that an integration of techniques is also needed to identify all network alterations caused by epilepsy and determine an 'epileptogenic network signature'. We propose the term epileptogenic network signature as the combination of network based biomarkers that are needed to establish a surgical strategy that leads to seizure freedom, thus a theoretical equivalent of the epileptogenic zone. The techniques to define this network signature include but are not limited to DWI based structural and SPES-based effective networks. Functional networks might be a useful addition because they act on different temporal and spatial scales than effective and structural networks [81]–[83]. Quantifying the coupling between structural, effective, and functional networks is important for the integration of these networks. We recommend to first quantify this coupling in the physiological parts of brain networks. We hypothesize that especially disruptions in the coupling could indicate network alterations caused by epilepsy [25], [77]. We recommend exploring these disruptions using homogeneous patient populations in terms of pathology and epilepsy location since these clinical variables are known to affect network topology [29].

Another promising tool to integrate effective, structural, and functional networks and establish a network based surgical strategy is the virtual brain project. The virtual brain models a patient-specific brain using functional and structural network data in a computational neuronal model [85]. With this model, the extent of the epileptogenic network signature could be estimated. Furthermore, seizures could be simulated which allows exploration of the seizure outcome of surgical strategies. With seizure simulation, new network based biomarkers could be experimentally validated without the need to validate network based biomarkers with estimates of the epileptogenic zone.

A future application of structural networks is in the planning of intracranial electrode locations. Whole-brain scale structural networks could be made to non-invasively determine network alterations and identify important nodes and connections in the epileptogenic networks. This first hypothesis of the epileptogenic network signature could then be confirmed during the iEEG monitoring period with effective networks and analysis of seizure propagation.

A different application for structural and effective networks lies in network modulation. Network modulation aims to disturb the epileptogenic network via vagal nerve stimulation, deep brain

stimulation, or cortical stimulation. The response to these treatments varies largely among patients and we do not completely understand why [86]. Insight into how neuromodulation affects effective networks, structural networks, and their relation might help us find the optimal stimulation settings and predict response to network modulation.

A network approach might also be useful in the earlier stages of epilepsy. Research showed that network alterations could clarify behavioral and cognitive deficits in epilepsy patients [87], [88]. Network analysis might identify patients at risk and help understand why these deficits arise.

5.3 Conclusion

We observed a moderate relation between structural networks and effective networks in overall overlap and topography. Both structural and effective networks hold future possibilities towards a network based surgical strategy. We recommend a multi-modality approach to study the complex network alterations in focal epilepsy patients.

6. References

[1] "Epilepsy." Available: https://www.who.int/news-room/fact-sheets/detail/epilepsy. [Accessed: 20-Aug-2022].

[2] "epilepsy - Search Results - PubMed." Available: https://pubmed.ncbi.nlm.nih.gov/?term=epilepsy&filter=datesearch.y_1. [Accessed: 20-Aug-2022].

[3] "Epilepsie | Volksgezondheid en Zorg." Available: https://www.vzinfo.nl/epilepsie. [Accessed: 20-Aug-2022].

[4] M. R. Sperling, "The consequences of uncontrolled epilepsy," *CNS Spectr.*, vol. 9, no. 2, 2004.

[5] P. Kwan *et al.*, "Definition of drug resistant epilepsy: consensus proposal by the ad hoc Task Force of the ILAE Commission on Therapeutic Strategies," *Epilepsia*, vol. 51, no. 6, pp. 1069–1077, 2010.

[6] H. J. Lamberink *et al.*, "Seizure outcome and use of antiepileptic drugs after epilepsy surgery according to histopathological diagnosis: a retrospective multicentre cohort study," *Lancet Neurol.*, vol. 19, no. 9, pp. 748–757, Sep. 2020.

[7] J. Engel, H. Luders, and C. Munari, *General principles*. 1993.

[8] O. David, A. S. Job, L. De Palma, D. Hoffmann, L. Minotti, and P. Kahane, "Probabilistic functional tractography of the human cortex," *Neuroimage*, vol. 80, pp. 307–317, Oct. 2013.

[9] R. P. Lesser, N. E. Crone, and W. R. S. Webber, "Subdural Electrodes," *Clin. Neurophysiol.*, vol. 121, no. 9, p. 1376, Sep. 2010.

[10] K. M. Grande, S. K. Z. Ihnen, and R. Arya, "Electrical Stimulation Mapping of Brain Function: A Comparison of Subdural Electrodes and Stereo-EEG," *Front. Hum. Neurosci.*, vol. 14, p. 538, Dec. 2020.

[11] R. Matsumoto *et al.*, "Functional connectivity in the human language system: a cortico-cortical evoked potential study," *Brain*, vol. 127, no. 10, pp. 2316–2330, Oct. 2004.

[12] R. Matsumoto, D. R. Nair, E. LaPresto, W. Bingaman, H. Shibasaki, and H. O. Lüders, "Functional connectivity in human cortical motor system: a cortico-cortical evoked potential study," *Brain*, vol. 130, no. 1, pp. 181–197, Jan. 2007.

[13] J. R. Alger, "The Diffusion Tensor Imaging Toolbox," *J. Neurosci.*, vol. 32, no. 22, p. 7418, May 2012.

[14] K. Tertel, N. Tandon, and T. M. Ellmore, "Probing Brain Connectivity by Combined Analysis of Diffusion MRI Tractography and Electrocorticography," *Comput. Biol. Med.*, vol. 41, no. 12, p. 1092, Dec. 2011.

[15] T. A. G. M. Huisman, "Diffusion-weighted and diffusion tensor imaging of the brain, made easy," *Cancer Imaging*, vol. 10, no. 1A, p. S163, 2010.

[16] D. Le Bihan, E. Breton, D. Lallemand, P. Grenier, E. Cabanis, and M. Laval-Jeantet, "MR imaging of intravoxel incoherent motions: application to diffusion and perfusion in neurologic disorders," *Radiology*, vol. 161, no. 2, pp. 401–407, 1986.

[17] V. Baliyan, C. J. Das, R. Sharma, and A. K. Gupta, "Diffusion weighted imaging: Technique and applications," *World J. Radiol.*, vol. 8, no. 9, p. 785, 2016.

[18] B. Jeurissen, A. Leemans, J. D. Tournier, D. K. Jones, and J. Sijbers, "Investigating the prevalence of complex fiber configurations in white matter tissue with diffusion magnetic resonance imaging," *Hum. Brain Mapp.*, vol. 34, no. 11, pp. 2747–2766, Nov. 2013.

[19] J. D. Tournier, F. Calamante, D. G. Gadian, and A. Connelly, "Direct estimation of the fiber orientation density function from diffusion-weighted MRI data using spherical deconvolution," *Neuroimage*, vol. 23, no. 3, pp. 1176–1185, Nov. 2004.

[20] "Spherical coordinates — pi2 documentation." Available: https://pi2-docs.readthedocs.io/en/latest/spherical_coordinates.html. [Accessed: 20-Aug-2022].

[21] J. D. Tournier, F. Calamante, and A. Connelly, "Robust determination of the fibre orientation distribution in diffusion MRI: non-negativity constrained super-resolved spherical deconvolution," *Neuroimage*, vol. 35, no. 4, pp. 1459–1472, May 2007.

[22] P. J. Basser, S. Pajevic, C. Pierpaoli, J. Duda, and A. Aldroubi, “In Vivo Fiber Tractography Using DT-MRI Data,” *Magn. Reson. Med.*, vol. 44, pp. 625–632, 2000.
[23] P. Mukherjee, J. I. Berman, S. W. Chung, C. P. Hess, and R. G. Henry, “Diffusion Tensor MR Imaging and Fiber Tractography: Theoretic Underpinnings,” *AJNR Am. J. Neuroradiol.*, vol. 29, no. 4, p. 632, Apr. 2008.
[24] J. Y. M. Yang, C. H. Yeh, C. Poupon, and F. Calamante, “Diffusion MRI tractography for neurosurgery: the basics, current state, technical reliability and challenges,” *Phys. Med. Biol.*, vol. 66, no. 15, p. 15TR01, Jul. 2021.
[25] C. S. Parker *et al.*, “Structural and effective connectivity in focal epilepsy,” *Neuroimage (Amst).*, vol. 17, p. 943, 2018.
[26] M. Mijalkov, E. Kakaei, J. B. Pereira, E. Westman, and G. Volpe, “BRAPH: A graph theory software for the analysis of brain connectivity,” *PLoS One*, vol. 12, no. 8, p. e0178798, Aug. 2017.
[27] D. van Blooijs, F. S. S. Leijten, P. C. van Rijen, H. G. E. Meijer, and G. J. M. Huiskamp, “Evoked directional network characteristics of epileptogenic tissue derived from single pulse electrical stimulation,” *Hum. Brain Mapp.*, vol. 39, no. 11, p. 4611, Nov. 2018.
[28] S. Boulogne *et al.*, “Functional connectivity and epileptogenicity of nodular heterotopias: A single-pulse stimulation study,” *Epilepsia*, vol. 63, no. 4, pp. 961–973, Apr. 2022.
[29] G. Slinger, W. M. Otte, K. P. J. Braun, and E. van Diessen, “An updated systematic review and meta-analysis of brain network organization in focal epilepsy: Looking back and forth,” *Neurosci. Biobehav. Rev.*, vol. 132, pp. 211–223, Jan. 2022.
[30] W. Jiang, J. Li, X. Chen, W. Ye, and J. Zheng, “Disrupted Structural and Functional Networks and Their Correlation with Alertness in Right Temporal Lobe Epilepsy: A Graph Theory Study,” *Front. Neurol.*, vol. 8, no. MAY, May 2017.
[31] B. C. Bernhardt *et al.*, “Temporal lobe epilepsy: Hippocampal pathology modulates connectome topology and controllability,” *Neurology*, vol. 92, no. 19, pp. E2209–E2220, May 2019.
[32] B. M. Campos *et al.*, “White matter abnormalities associate with type and localization of focal epileptogenic lesions,” *Epilepsia*, vol. 56, no. 1, pp. 125–132, Jan. 2015.
[33] A. Valentín *et al.*, “Responses to single pulse electrical stimulation identify epileptogenesis in the human brain in vivo,” *Brain*, vol. 125, no. Pt 8, pp. 1709–1718, 2002.
[34] R. Matsumoto, T. Kunieda, and D. Nair, “Single pulse electrical stimulation to probe functional and pathological connectivity in epilepsy,” *Seizure*, vol. 44, pp. 27–36, Jan. 2017.
[35] A. Valentín *et al.*, “Responses to single pulse electrical stimulation identify epileptogenesis in the human brain in vivo,” *Brain*, vol. 125, no. Pt 8, pp. 1709–1718, 2002.
[36] R. Matsumoto *et al.*, “Parieto-frontal network in humans studied by cortico-cortical evoked potential,” *Hum. Brain Mapp.*, vol. 33, no. 12, pp. 2856–2872, Dec. 2012.
[37] R. Enatsu *et al.*, “Connections of the limbic network: A corticocortical evoked potentials study,” *Cortex*, vol. 62, pp. 20–33, Jan. 2015.
[38] B. H. Silverstein, E. Asano, A. Sugiura, M. Sonoda, M. H. Lee, and J. W. Jeong, “Dynamic tractography: Integrating cortico-cortical evoked potentials and diffusion imaging,” *Neuroimage*, vol. 215, p. 116763, Jul. 2020.
[39] D. van Blooijs, “Improving the SPES protocol by automating ER and DR detection and evaluation of the spatial relation between ERs and DRs - MSc Thesis,” University of Twente, Enschede, 2015.
[40] D. Prime, D. Rowlands, S. O’Keefe, and S. Dionisio, “Considerations in performing and analyzing the responses of cortico-cortical evoked potentials in stereo-EEG,” *Epilepsia*, vol. 59, no. 1, pp. 16–26, 2018.
[41] M. L. McHugh, “Interrater reliability: the kappa statistic,” *Biochem. Medica*, vol. 22, no. 3, p. 276, 2012.
[42] K. H. Zou, C. R. Yu, K. Liu, M. O. Carlsson, and J. Cabrera, “Optimal thresholds by maximizing or minimizing various metrics via ROC-type analysis,” *Acad. Radiol.*, vol. 20, no. 7, pp. 807–815,

Jul. 2013.
[43] L. Trebaul *et al.*, “Probabilistic functional tractography of the human cortex revisited,” *Neuroimage*, vol. 181, pp. 414–429, Nov. 2018.
[44] T. Mitsuhashi, M. Sonoda, H. Iwaki, A. F. Luat, S. Sood, and E. Asano, “Effects of depth electrode montage and single-pulse electrical stimulation sites on neuronal responses and effective connectivity,” *Clin. Neurophysiol.*, vol. 131, no. 12, pp. 2781–2792, Dec. 2020.
[45] M. W. Watkins and M. Pacheco, “Interobserver Agreement in Behavioral Research: Importance and Calculation,” *J. Behav. Educ. 2000 104*, vol. 10, no. 4, pp. 205–212, 2000.
[46] B. Frauscher *et al.*, “Atlas of the normal intracranial electroencephalogram: neurophysiological awake activity in different cortical areas,” *Brain*, vol. 141, no. 4, pp. 1130–1144, Apr. 2018.
[47] K. H. Maier-Hein *et al.*, “The challenge of mapping the human connectome based on diffusion tractography,” *Nat. Commun. 2017 81*, vol. 8, no. 1, pp. 1–13, Nov. 2017.
[48] C. R. Conner, T. Ellmore, M. A. DiSano, T. A. Pieters, A. Potter, and N. Tandon, “Anatomic and electro-physiologic connectivity of the language system: a combined DTI-CCEP study,” *Comput. Biol. Med.*, vol. 41, no. 12, p. 1100, Dec. 2011.
[49] N. C. Swann *et al.*, “Roles for the pre-supplementary motor area and the right inferior frontal gyrus in stopping action: Electrophysiological responses and functional and structural connectivity,” *Neuroimage*, vol. 59, no. 3, pp. 2860–2870, 2012.
[50] P. Filipiak *et al.*, “Towards linking diffusion MRI based macro- and microstructure measures with cortico-cortical transmission in brain tumor patients,” *Neuroimage*, vol. 226, p. 117567, Feb. 2021.
[51] B. Crocker *et al.*, “Local and distant responses to single pulse electrical stimulation reflect different forms of connectivity,” *Neuroimage*, vol. 237, p. 118094, Aug. 2021.
[52] T. Mitsuhashi *et al.*, “Four-dimensional tractography animates propagations of neural activation via distinct interhemispheric pathways,” *Clin. Neurophysiol.*, vol. 132, no. 2, pp. 520–529, Feb. 2021.
[53] E. Kaufmann, J. Bartkiewicz, N. Fearns, K. Ernst, C. Vollmar, and S. Noachtar, “Unilateral Blinking: Insights from Stereo-EEG and Tractography,” *Brain Topogr.*, vol. 34, no. 5, pp. 698–707, Sep. 2021.
[54] A. C. Waters *et al.*, “Test–retest reliability of a stimulation-locked evoked response to deep brain stimulation in subcallosal cingulate for treatment resistant depression,” *Hum. Brain Mapp.*, vol. 39, no. 12, pp. 4844–4856, Dec. 2018.
[55] R. E. Smith, J. D. Tournier, F. Calamante, and A. Connelly, “Anatomically-constrained tractography: improved diffusion MRI streamlines tractography through effective use of anatomical information,” *Neuroimage*, vol. 62, no. 3, pp. 1924–1938, Sep. 2012.
[56] J. D. Tournier, F. Calamante, and A. Connelly, “MRtrix: Diffusion tractography in crossing fiber regions,” *Int. J. Imaging Syst. Technol.*, vol. 22, no. 1, pp. 53–66, Mar. 2012.
[57] M. Demuru, D. van Blooijs, W. Zweiphenning, D. Hermes, F. Leijten, and M. Zijlmans, “A Practical Workflow for Organizing Clinical Intraoperative and Long-term iEEG Data in BIDS,” *Neuroinformatics*, vol. 1, pp. 1–10, Mar. 2022.
[58] “MRtrix3.” [Online]. Available: https://www.mrtrix.org/. [Accessed: 30-Nov-2021].
[59] J. Veraart, D. S. Novikov, D. Christiaens, B. Ades-aron, J. Sijbers, and E. Fieremans, “Denoising of diffusion MRI using random matrix theory,” *Neuroimage*, vol. 142, pp. 394–406, Nov. 2016.
[60] E. Kellner, B. Dhital, V. G. Kiselev, and M. Reisert, “Gibbs-ringing artifact removal based on local subvoxel-shifts,” *Magn. Reson. Med.*, vol. 76, no. 5, pp. 1574–1581, Nov. 2016.
[61] J. L. R. Andersson, S. Skare, and J. Ashburner, “How to correct susceptibility distortions in spin-echo echo-planar images: Application to diffusion tensor imaging,” *Neuroimage*, vol. 20, no. 2, pp. 870–888, Oct. 2003.
[62] J. L. R. Andersson and S. N. Sotiropoulos, “An integrated approach to correction for off-resonance effects and subject movement in diffusion MR imaging,” *Neuroimage*, vol. 125, pp. 1063–1078, Jan. 2016.

[63] N. J. Tustison *et al.*, “N4ITK: Improved N3 bias correction,” *IEEE Trans. Med. Imaging*, vol. 29, no. 6, pp. 1310–1320, Jun. 2010.
[64] J. D. Tournier, F. Calamante, and A. Connelly, “Robust determination of the fibre orientation distribution in diffusion MRI: Non-negativity constrained super-resolved spherical deconvolution,” *Neuroimage*, vol. 35, no. 4, pp. 1459–1472, May 2007.
[65] M. Descoteaux, “High Angular Resolution Diffusion Imaging (HARDI),” *Wiley Encycl. Electr. Electron. Eng.*, pp. 1–25, Jun. 2015.
[66] B. Ter *et al.*, “Extrapolating fiber crossings from DTI data. Can we gain similar information as HARDI? ,” 2010.
[67] F. C. Yeh *et al.*, “Population-averaged atlas of the macroscale human structural connectome and its network topology,” *Neuroimage*, vol. 178, pp. 57–68, Sep. 2018.
[68] D. Perrone *et al.*, “D-BRAIN: Anatomically Accurate Simulated Diffusion MRI Brain Data,” *PLoS One*, vol. 11, no. 3, Mar. 2016.
[69] H. Takemura, C. F. Caiafa, B. A. Wandell, and F. Pestilli, “Ensemble Tractography,” *PLOS Comput. Biol.*, vol. 12, no. 2, p. e1004692, Feb. 2016.
[70] W. Wu *et al.*, “High-resolution diffusion MRI at 7T using a three-dimensional multi-slab acquisition,” *Neuroimage*, vol. 143, p. 1, Dec. 2016.
[71] B. Ades-Aron *et al.*, “Evaluation of the accuracy and precision of the diffusion parameter EStImation with Gibbs and NoisE removal pipeline,” *Neuroimage*, vol. 183, pp. 532–543, Dec. 2018.
[72] T. Dhollander, R. Mito, and D. Raffelt, “ Improved white matter response function estimation for 3-tissue constrained spherical deconvolution,” in *Proceedings of the 27th annual meeting of the International Society of Magnetic Resonance in Medicine*, 2019, p. 555.
[73] N. C. Chung, B. Z. Miasojedow, M. Startek, and A. Gambin, “Jaccard/Tanimoto similarity test and estimation methods for biological presence-absence data,” *BMC Bioinformatics*, vol. 20, no. 15, pp. 1–11, Dec. 2019.
[74] “R Core Team.” 2022.
[75] G. Leng, “The endocrinology of the brain,” *Endocr. Connect.*, vol. 7, no. 12, p. R275, 2018.
[76] G. Schiera, C. M. Di Liegro, and I. Di Liegro, “Cell-to-Cell Communication in Learning and Memory: From Neuro- and Glio-Transmission to Information Exchange Mediated by Extracellular Vesicles,” *Int. J. Mol. Sci.*, vol. 21, no. 1, Jan. 2020.
[77] E. Van Diessen, S. J. H. Diederen, K. P. J. Braun, F. E. Jansen, and C. J. Stam, “Functional and structural brain networks in epilepsy: What have we learned?,” *Epilepsia*, vol. 54, no. 11, pp. 1855–1865, Nov. 2013.
[78] M. Demuru *et al.*, “Validation of virtual resection on intraoperative interictal data acquired during epilepsy surgery,” *J. Neural Eng.*, vol. 17, no. 6, Nov. 2020.
[79] J. Hebbink, H. Meijer, G. Huiskamp, S. van Gils, and F. Leijten, “Phenomenological network models: Lessons for epilepsy surgery,” *Epilepsia*, vol. 58, no. 10, pp. e147–e151, Oct. 2017.
[80] A. Schippers, M. J. Vansteensel, Z. V. Freudenburg, F. S. S. Leijten, and N. F. Ramsey, “Detailed somatotopy of tongue movement in the human sensorimotor cortex: A case study,” *Brain Stimul.*, vol. 14, no. 2, pp. 287–289, Mar. 2021.
[81] M. Liu, Z. Chen, C. Beaulieu, and D. W. Gross, “Disrupted anatomic white matter network in left mesial temporal lobe epilepsy,” *Epilepsia*, vol. 55, no. 5, pp. 674–682, May 2014.
[82] Y. Li Hegner *et al.*, “Increased Functional MEG Connectivity as a Hallmark of MRI-Negative Focal and Generalized Epilepsy,” *Brain Topogr.*, vol. 31, no. 5, pp. 863–874, Sep. 2018.
[83] E. Mazzucchi *et al.*, “Hyperventilation in Patients With Focal Epilepsy: Electromagnetic Tomography, Functional Connectivity and Graph Theory - A Possible Tool in Epilepsy Diagnosis?,” *J. Clin. Neurophysiol.*, vol. 34, no. 1, pp. 92–99, 2017.
[84] M. G. Preti and D. Van De Ville, “Decoupling of brain function from structure reveals regional behavioral specialization in humans,” *Nat. Commun. 2019 101*, vol. 10, no. 1, pp. 1–7, Oct. 2019.
[85] S. Olmiid, S. Petkoskiid, M. Guyeid, F. Bartolomei, and V. Jirsa, “Controlling seizure

propagation in large-scale brain networks," 2019.
[86] D. H. Li and X. F. Yang, "Remote modulation of network excitability during deep brain stimulation for epilepsy," *Seizure*, vol. 47, pp. 42–50, Apr. 2017.
[87] M. C. G. Vlooswijk *et al.*, "Memory processes and prefrontal network dysfunction in cryptogenic epilepsy," *Epilepsia*, vol. 52, no. 8, pp. 1467–1475, Aug. 2011.
[88] M. J. Vaessen *et al.*, "Functional and Structural Network Impairment in Childhood Frontal Lobe Epilepsy," *PLoS One*, vol. 9, no. 3, Mar. 2014.

Appendix A

The analogy between structural networks obtained from diffusion weighted imaging and effective networks derived from single pulse electrical stimulation in people with epilepsy

S.B. Jelsma[1,2], D. van Blooijs[2,3], M.J.A.M. van Putten[1], M. Raemaekers[2], M. Zijlmans[2,4], N.E.C van Klink[2] , on behalf of the RESPect database group

1. MIRA Institute for Biomedical Engineering and Technical Medicine, University of Twente, Enschede, the Netherland
2. Brain Center, University Medical Center Utrecht, the Netherlands
3. Stichting Epilepsie Instellingen Nederland (SEIN), Zwolle, the Netherlands
4. Stichting Epilepsie Instellingen Nederland (SEIN), Heemstede, the Netherlands

Purpose: Epilepsy is regarded as a network disorder. Effective networks describe the connections between brain regions by perturbation of one region e.g., by single pulse electrical stimulation (SPES). Structural networks describe the connections between brain regions via white matter tracts derived from diffusion weighted imaging (DWI). We studied the similarity between these structural and effective networks. Comparison of the presence and strength of patient-specific connections between modalities can expand our knowledge of epileptogenic networks.

Method: We included patients who underwent DWI and long-term intracranial EEG monitoring with subdural electrocorticography (ECoG) or stereoEEG (sEEG). An automatic detector was optimized to detect early responses from SPES (0.2Hz, 10 stimuli) for both ECoG and sEEG. Effective networks were constructed with electrode contacts representing the nodes. Edges were drawn from the stimulus pair to the electrodes with early responses. DWI was acquired with 62 diffusion directions (b=1600s/mm^2)**.** Anatomical constrained probabilistic fiber tractography using constrained spherical deconvolution was performed with electrode contacts as regions of interest. Structural networks were constructed by the streamline density as edge between regions of interest. We will compare both networks with the Jaccard index and graph measures (degree, betweenness centrality, clustering coefficient) in- and outside epileptogenic tissue.

Results: We included 15 patients (six ECoG, eight sEEG, one sEEG+ECoG). The SPES-detector had a sensitivity of 82% and 78% and specificity of 82% and 91% for sEEG and ECoG data respectively. The networks had 56-154 nodes per patient (median: 84). The epileptogenic zone was covered by 3-37 electrodes (median: 10).

Conclusion: We designed a method to reveal complementary network characteristics of structural and effective patient-specific brain networks for sEEG and ECoG.